Aggregation and Dendrimer Mediated Secondary Binding towards Folate Binding Protein &

Fatigue Failure Mechanism of Anterior Cruciate Ligament Fracture

by

Junjie Chen

A dissertation submitted in partial fulfillment
of the requirements for the degree of
Doctor of Philosophy
(Chemistry)
in the University of Michigan
2018

Doctoral Committee:

Prof. Mark Banaszak Holl, co-chair
Prof. Neil Marsh, co-chair
Prof. Bradford Orr
Prof. Ayyalusamy Ramamoorthy

Junjie Chen

junjchen@Umich.edu

ORCID iD: 0000-0001-8004-8159

DEDICATION

For my family, my wife and my advisors

Acknowledgements

This work won't be possible without the help from my advisor, Dr. Mark Banaszak Holl. Mark is always accessible to his students to talk about science and even other life advices. As one of the greatest mentors at the University of Michigan, Mark always keeps his door open for students whenever he is available. Mark forwarded many great opportunities including paper review, paper invitation and internships, all of which benefitted my career. Mark is very patient on my growth and tolerated the tons of stupid mistakes/accidents I made in the past five years. When I was a GSI but got stuck in China due to delayed visa in winter 2016, Mark even taught for me for one week. I also learned the "smell of science" in the Banaszak Holl lab – how to set up scientific a question to answer; how to support your hypothesis with the "one-million control" and how to translate your result to the science community. Michigan lost a great professor and I feel that Monash University is extremely lucky to have Mark joining their team in 2018.

The Banaszak Holl group members have created a fun and collaborative atmosphere throughout my PhD. Rachel Merzel, who entered the group in the same year with me, had a deep collaboration on countless experiments. To date, we have published four papers together, ranging from dendrimer conjugation to protein aggregation, and to animal test on drug delivery. Rachel leaves a significant impact on at least half of my PhD.

I also need to thank Dr. Casey Dougherty and Dr. Sriram Vaidyanathan for providing the helps and suggestions early in my PhD. Jinhee Kim is my major collaborator on chapter 3 and she helped establish the understanding of ACL damage. I am also grateful for Isabel Colon-Bernal and Ted Ahn for maintaining the lab environment and equipment.

I can't be more grateful for my other committee members and my collaborators. Dr. Orr, who attends group meetings throughout my PhD, gave numerous helpful suggestions on polishing my work and leading to publications. Dr. Marsh provided extensive support in all the protein related material in this thesis as well as the collaboration opportunity on protein cages with Ajitha Cristie-David. Dr. Ramamoorthy provided NMR support for many projects and the opportunity to work on lipid nano-disks. I also initiated many collaborations with many talented people on campus. It was my hornor to publish with Dr. Zhan Chen, Minyu Xiao, Dr. Wojtys, Dr. Schlecht, Dr. Ashton Miller, and Haiye Wang et al. I learned additional skills/knowledge from those collaboration and those fun experience are one of the most rewarding things I got in graduate school.

The staff and researchers at University of Michigan provided all the equipment and support to make everything possible. The Department of Chemistry staff created a safe and convenient working environment for my study. The Michigan Nanotechnology Institute

for Medicine and Biological Sciences (MNIMBS) provided many technical support for the instrument and special thanks to Dr. Pamela Wong.

My parents have been very supportive both mentally and financially of me studying abroad. I felt deeply sorry for only visiting home once in my past four and half years. I wish I could spend more time with them and give my full support back to them in the future. Youfei, my fiancé, offered some of the happiest moments as I forged through the final years of my PhD. I am looking forward to forming the future family with Youfei and potentially, a collaborative scientific paper together.

Table of Contents

List of Figures

Abstract

Drug conjugation gives many advantages such as improved targeting, solubility and retention. How conjugated drugs interact with proteins is a key question to answer in targeted drug delivery. This not only includes the interaction with the target protein, but also includes the proteins that the drug carrier may encounter during drug trafficking. Folic acid (FA) is of wide interest as a targeting agent. It provides targeting effect towards the folate receptor (FR), a commonly overexpressed protein in breast cancer and ovarian cancer. Chapter one focused on developing a conjugated tighter binder towards the soluble form of folate receptor, folate binding protein (FBP). This strategy employed a PAMAM dendrimer conjugated folic acid; the dissociation constant was improved from 20 nM of free folic acid to 2 nM of the dendrimer conjugated folic acid. The folate binding protein is a minor serum protein and is known to aggregate upon binding to folic acid. This aggregation could pose risk factors for drug delivery vectors such as the folic acid conjugated iron oxide nanoparticles. In chapter two, folate binding protein was shown to aggregate to large iron oxide nanoparticles that are conjugated to folic acid, triggering the agglomeration cascade that could drastically change the size of these nanoparticles.

Chapter three addresses a question that is important to sport medicine: what leads to non-contact anterior cruciate ligament (ACL) failure? Our hypothesis was that before

the ACL fracture, microdamage would have already been created by jumping and landing activities. In this chapter, paired cadaveric knees were collected and one of the pair was mechanically tested under submaximal loading to see to what extent the microdamage would be created. A hierarchical damage ranging from nanometer level to micrometer level were detected using various methods including atomic force microscopy (AFM), nanoIR, second harmonic generation (SHG) and confocal microscopy. These microdamages exhibits patterns that resemble the fractured ACL seen in the clinical patients.

Chapter I

Enhanced Folate Binding Protein Avidity: a Two Step Process Mediated by Dendrimer Exosite Binding

Introduction

Polymer-ligand conjugates are designed to bind protein active sites for applications as drugs, imaging agents, and transport scaffolds.[1-3] The polymer provides many potential advantages including increasing ligand solubility, enhancing the circulation time, and shielding the ligand from unwanted protein interactions. These strategies have been successfully implemented for mono-functional poly(ethyleneglycol) (PEG) polymers and translated into successful drugs in the clinic.[4] In principle, polymer scaffolds can also be employed to improve ligand to protein binding. However, the major strategy employed in this regard, multivalent display of the ligand, has failed to realize the theoretically achievable improvements in binding.[5-6]

Vitamins are particularly attractive molecules for drug targeting since they are naturally occurring, often exhibit low toxicity and high stability in plasma and tissue, and are preferentially taken up by quickly replicating cancer cells.[7] Substantial effort has been expended to develop polymer conjugates of vitamins for use in targeting and imaging cancer cells. In particular, vitamin B_9 or folic acid (FA) has received extensive attention in this regard, and seven molecular conjugates have advanced to clinical trials.[7] Despite great promise, FA-conjugates have not yet advanced to clinic. Polymer conjugates of FA

have also been extensively explored including multivalent display of the ligand to enhance total binding strength and/or selectivity to displays of FA receptors.[8-9]

Figure 1.1 Synergistic exosite binding mechanism. The α–helix and β–sheet secondary structure formed upon FA binding is highlighted purple in the X-ray crystal structure below.

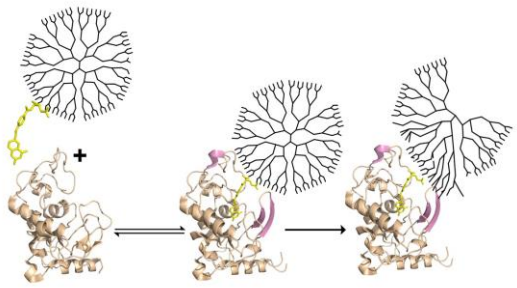

We now report a new strategy to achieve tight polymer-ligand conjugate binding to target proteins by exploiting polymer-protein interactions. The strategy employs substrate-triggered exosite binding of the protein and polymer surfaces. It is known that FA induces changes in the secondary structure of FBP upon binding, including the formation of new domains of α–helix and β–sheet and rearrangement of a loop near the entrance to the binding site.[10] We show that after these structural changes have been triggered by binding, the generation five poly(amidoamine) (G5 PAMAM) dendrimer conjugated to the FA interacts with the protein surface. This new exosite interaction results in strong binding of the ligand-dendrimer conjugate to FBP. The polymer-conjugate/exosite binding strategy is potentially useful as it offers specificity of interaction based on the natural protein ligand. This strong, tight binding could be of substantial benefit for FA-conjugated imaging agents. Figure 1.1 illustrates the proposed binding mechanism with the induced α–helix and β–sheet highlighted.

Folate binding protein (FBP) describes two membrane-bound isoforms of the protein: folate receptor alpha (FR-α) and folate receptor beta (FR-β) that are linked to plasma cell membranes via glycosylphosphatidylinositol (GPI) anchors.[11-12] There is also a secreted form, FR-γ, that lacks the GPI anchor. All forms of the protein have molecular

weights at around 30 kDa. Soluble FBP, present at 1-2 nM concentration in human serum and other body fluids and 100 nM concentrations in milk,[12-17] is believed to be a mixture of FR-γ and FR-α that has undergone cleavage of the GPI anchor. X-ray crystal structures of FA-bound FR-α and FA-bound FR-β were recently reported.[10, 18] In the studies reported here, we employed bovine FBP (bFBP) isolated from milk. bFBP has overall >80% homology with human FR-α (hFR-α). In particular, there is 100% homology for 21 key residues forming the FA binding pocket, which includes the –QSWRKERVL- section of the inner strand of the nascent β–sheet that forms upon FA binding.

Experimental Section

Materials. PEG-FA conjugates (2k, 5k, 30k) were purchased from Nanocs Inc. G5 PAMAM dendrimer was purchased from Dendritech and purified to remove trailing generation and G5 oligomer impurities as previously reported.[19] $G5_{Ac}$-COG-$FA_{1.0}$ (credit: Mallory A. van Dongen, Ananda Kumar Kanduluru, Philip S. Low)[20] and $G5_{Ac}$-$FITC_{1.9}$-$FA_{4.4}$ (credit: Rachel L. Merzel, Casey A. Dougherty) were synthesized according to previously reported methods.[21-22] All dendrimers used have the primary amine terminal groups acetylated (Ac) to avoid protonation in aqueous buffer. Whey protein concentrate was purchased from Natural Foods Inc. and purified as briefly described below following previously reported methods.[23] All other chemicals and materials were purchased from Sigma-Aldrich or Fischer Scientific and used as received.

Extraction, Purification, and Activity of FBP

A 200 mL bed volume of Sepharose 4B was activated by cyanogen bromide and subsequently conjugated to FA. A pH 7.0 2% (w/v) whey protein solution was centrifuged

(20,000 g) for 20 minutes. The resulting supernatant was loaded on the FA affinity column. 10 L of supernatant was run through the column prior to the onset of back-pressure. Unbound protein was washed away using 2 L of 1 M NaCl followed until the solution ran clear using at least 2L of nanopure water. 300 mL of 0.3 M acetic acid solution was used to flush the FBP off the column. The solution was collected by fractions. Fractions with 90% FBP purity were combined and the pH was adjusted to 7.0 by the addition of 5.0 M NaOH.

Fluorescence Measurements

All fluorescence measurements were carried out on a Varian Cary Eclipse Fluorescence Spectrophotometer. A 58 nM folate binding protein solution was made in pH 7.4 1x PBS. The temperature control was set at 22 °C. Excitation wavelengths of 280 nm for tryptophan and 495nm for FITC were employed. The slit widths were 8 nm for both excitation and emission monochromators. In all cases, fluorescence measurements were taken after the solutions had reached an equilibrium value.

Results and Discussion

In previous surface plasmon resonance (SPR) studies of G5-FA/FBP binding, we discovered that G5-FA_n (n = 1, 2 or various n_{avg}) bound essentially irreversibly to bFBP.[20, 24] Using atomic force microscopy (AFM) force-pulling studies, we found that the most probable rupture forces were 83, 201, and 189 pN for G5-$FA_{2.7}$, G5-$FA_{4.7}$, and G5-$FA_{7.2}$, respectively.[25] Intriguingly, although the probability of interaction decreased with FA-blocking, the force magnitude of the most probable rupture force increased from 189 to 274 pN for G5-$FA_{7.2}$. The combination of the SPR and AFM force-pulling data is

Figure 1.2. G5 PAMAM and PEG FA-conjugates employed in this study.

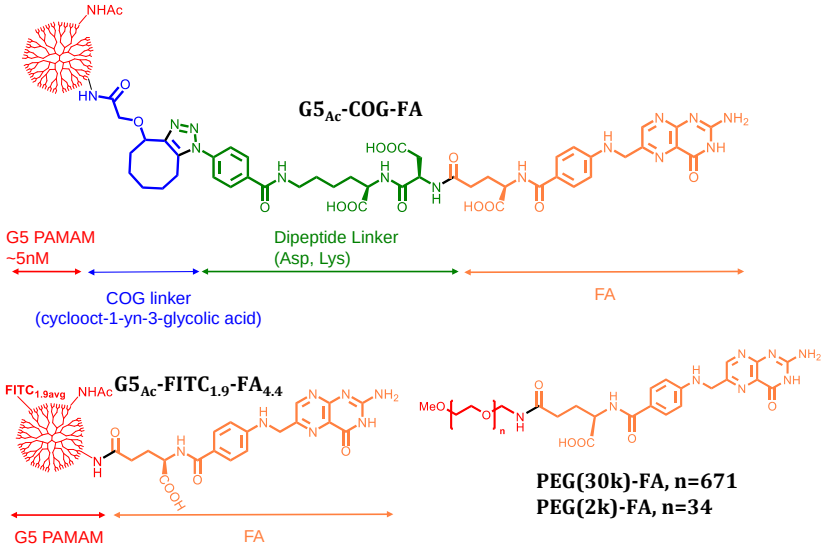

consistent with a slow-onset, tight-binding (SOTB) FA/FBP binding mechanism where FA-binding induces significant structural change in the bFBP secondary structure, allowing a network of van der Waals interactions to form between the G5 PAMAM dendrimer surface and the bFBP surface. [20, 25]

The interaction between polymer backbones and proteins is considered to be the most important factor in polymer-based drug delivery and biodevice development.[26] Proteins have been shown to interact with polymers via a complex set of interactions that include generalised electrostatic,[27] van der waals,[28] and H-bonding[29] interactions and more specific protein-polymer binding.[30] These interactions have generally been studied in the context of protein adsoprtion onto surfaces as opposed to the triggered exosite binding described herein.

To further explore the nature of these interactions, we have performed a series of solution-phase fluorescence quenching experiments taking advantage of the intrinsic fluorescence associated with the 11 tryptophan residues present in bFBP. For these studies,

we employed the following FA-polymer conjugates: 1) FA stochastically conjugated to a terminal PAMAM amine group (Figure 1.2, $G5_{Ac}$ -$FITC_{1.9}$-$FA_{4.4}$). This provides a direct comparison to our initial SPR[24] and force-pulling[25] studies and other stochastic FA conjugations for G5 PAMAM reported in the literature;[8, 31-34] 2) A G5-FA conjugate containing precisely one FA molecule per G5 PAMAM polymer ($G5_{Ac}$-COG-$FA_{1.0}$). This eliminates any effects arising from multivalent FA interactions including bridging between two bFBP. Recent SPR studies on $G5_{Ac}$-COG-$FA_{1.0}$ led to the proposed SOTB interaction for G5-FA/FBP binding;[20] 3) FA-PEG conjugates directly linked via a FA carboxylic acid to the terminal PEG amine. The 30 kDA PEG (PEG_{30k}-FA) was chosen to provide an equivalent MW to that of acetylated $G5_{Ac}$ PAMAM. The 2 kDa PEG (PEG_{2k}-FA) was chosen to provide a PEG conjugate with less steric bulk.

Fluorescence Quenching of bFBP upon FA and FA-conjugate Binding

Fluorescence quenching titration provides a high sensitivity method for studying biological processes due to its high sensitivity.[35] However when employing this technique to make quantitative measurements, it is important to correct for inner filter effects (IFE) and dynamic quenching that can decrease the observed light

Figure 1.3. Modified Stern-Volmer fitting of tryptophan quenching curves after the conjugation. ●$G5_{Ac}$, ■ PEG_{2k}-COG-FA(mix) ,▲PEG_{30k}-FA, ▼PEG_{2k}-FA, ◆$G5_{Ac}$-$FITC_{1.9}$-$FA_{4.4}$, ○FA, □ $G5_{Ac}$-COG-FA.

The concentration of FBP in each case is 58 nM (pH 7.4, 1x PBS solution).

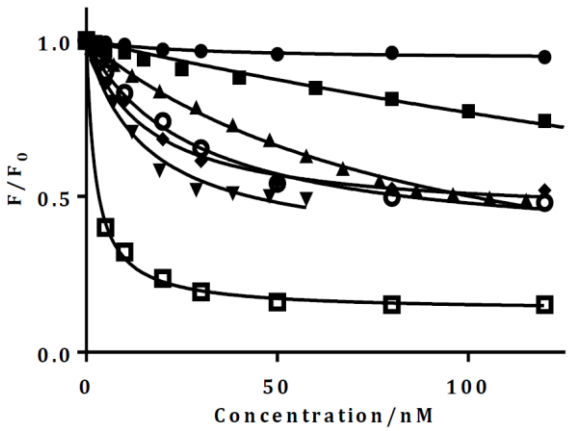

Figure 1.4. Locations of tryptophans (green and red) and bound FA (yellow) in hFR-α. W171 & W102 (bottom) are highlighted in red.

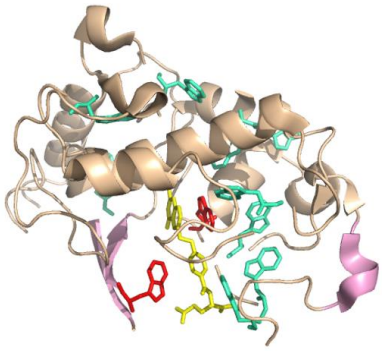

intensity.[36] At the submicromolar concentrations of titrant employed for these studies, IFE did not cause an observable effect in light intensity for any of the polymer conjugates.

Titration of a 58 nM FBP solution with FA results in a roughly 50% quenching of the native tryptophan fluorescence (Figure 1.3). This experiment was suggested by Dr. E Neil G Marsh. A comparison of the apo-FPB and FA-FBP X-ray structures indicates that the majority of the tryptophan residues do not change position upon FA binding.[10] Notable exceptions are W171, which is located on the protein surface away from the FA binding site, and W102, which is located on the loop adjacent to the FA-binding site and plays a key role in FA binding and β–sheet formation (Figure 1.4). The distance between W102 and the FA benzamide ring (5.1 Å, 15° angle) is consistent with parallel-displaced π-π stacking.[10] Tryptophan W171 is also of particular interest as it π-stacks with FA pteridine ring (3.7 Å, 15° angle). W64, 120 134, 138, and 140, all located along the FA binding site, are highlighted in green in Figure 1.4. Titration with $G5_{Ac}$-$FITC_{1.9}$-$FA_{4.4}$ resulted in a similar quenching level to that observed for free FA (Figure 1.3). Surprisingly, titration with $G5_{Ac}$-COG-$FA_{1.0}$ resulted in roughly 80% fluorescence quenching and exhibits a steeper initial slope indicating a different stoichiometry of interaction. Treatment of FBP with free FA, followed by addition of acetylated G5 dendrimer ($G5_{Ac}$), resulted in no additional fluorescence quenching. This result indicates that for the enhanced fluorescence

quenching to occur the dendrimer must be conjugated to FA. Thus, synergistic binding requires both FA-induced FBP structural change and FA conjugation to the dendrimer.

In order to explore the role of polymer in the binding process, studies were carried out with PEG_{30k}-FA and PEG_{2k}-FA. As illustrated in Figure 1.3, titration of FBP with PEG_{30k}-FA or PEG_{2k}-COG-FA resulted in only about 20% fluorescence quenching and had not yet reached saturation by 120 nM of added conjugate. This data demonstrates the equilibrium binding shift expected for conjugates that have steric constraints to achieving FA-FBP binding. The PEG_{2k}-FA exhibits similar quenching to free FA whereas PEG_{30k}-FA requires a roughly 2-fold greater concentration to achieve saturated binding. PEG_{2k}-COG-FA binds less effectively than PEG_{2k}-FA suggesting that the COG linker is increasing steric constraints in this case. This is an important control as it demonstrates that the presence of the triazole ring/tryptophan interactions do not induce the large amount of quenching observed for $G5_{Ac}$-COG-$FA_{1.0}$. The PEG-FA conjugates demonstrate the typical result of polymer conjugation to a protein binding substrate, namely, equivalent binding or reduced binding caused by steric constraints. The results provide a distinct contrast to the binding interaction of $G5_{Ac}$-COG-$FA_{1.0}$ with FBP where a dramatic increase in binding constant[20] and fluorescence quenching is observed.

The fluorescence quenching curves were fit to the modified Stern-Volmer equation to assess binding avidity of polymer conjugates to FBP. [37]

$$\frac{I}{I_0} = 1 - \frac{f_a[\mathrm{Q}]}{K_D + [\mathrm{Q}]}$$

Figure 1.5. Tight binding of $G5_{Ac}$-COG-$FA_{1.0}$ to FBP. A) Fluorescence quenching of 58 nM FBP in the presence of 800nM FA B) 80 nM $G5_{Ac}$-COG-$FA_{1.0}$ binds to FBP, displacing FA, in the presence of excess FA. C) The presence of an additional 800nM excess FA does not displace $G5_{Ac}$-COG-$FA_{1.0}$. The FBP concentration is 58 nM (pH 7.4, 1x PBS solution).

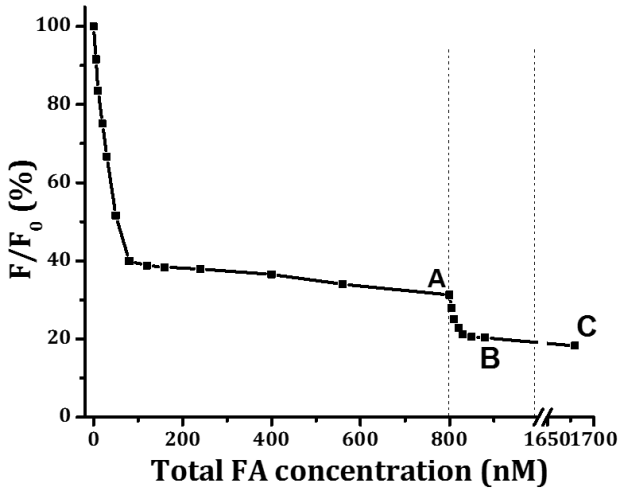

I is the intensity of the fluorophore, f_a is the fraction of accessible fluorophores, K_D is the dissociation constant, and *[Q]* is the free titrant concentration calculated from a quadratic equation (Scheme S1).[38] A static quenching effect from binding was observed from the fitting. The plots (Figure 1.3) yield K_D = 27.9 ± 3.3 nM for FBP binding FA, similar to the literature value of 20 nM,[39] whereas the $G5_{Ac}$-COG-$FA_{1.0}$ conjugate bound FBP with K_D = 2.43 ± 0.17 nM, roughly ten-fold more tightly than FA. The PEG_{30k}-FA isotherm bound with K_D = 51.4 ± 6.4 nM, indicating that the polymer plays a relatively small role in modulating the binding avidity to FBP. $G5_{Ac}$-COG-$FA_{1.0}$ quenches a larger fraction of accessible fluorophores (f_a = 87 ± 1%) as compared to FA (f_a = 67 ± 3%) or PEG_{30k}-FA (f_a = 66 ± 4%). This is presumably an indication of the large conformational change induced by the dendrimer binding to the exosite on the protein surface.

The binding avidity comparison of FA/FBP and $G5_{Ac}$-COG-$FA_{1.0}$/FBP was tested by first saturating FBP with 14 equiv FA (Figure 1.5). The subsequent addition of 1.4

Figure 1.6 Tryptophan fluorescence from FBP a) Tryptophan fluorescence from FBP in the presence of folic acid (FA) and $G5_{Ac}$-$FITC_{1.9}$-$FA_{4.4}$ conjugate, ex: 280nm b) FITC fluorescence from $G5_{Ac}$ -$FITC_{1.9}$-$FA_{4.4}$ in the presence of folic acid (FA) and FBP, ex: 495nm. The concentration of FBP in each case was 58 nM (pH 7.4, 1x PBS solution).

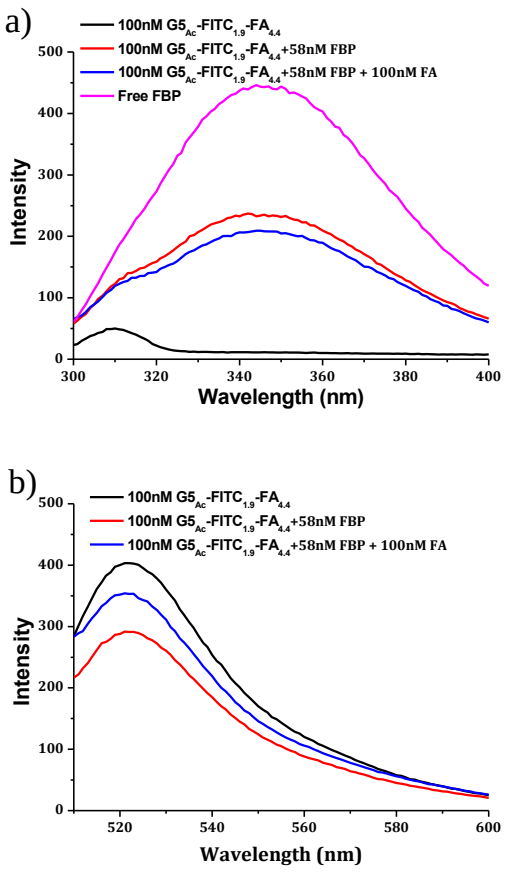

equiv $G5_{Ac}$-COG-$FA_{1.0}$ induced additional quenching to the 80% level previously observed for $G5_{Ac}$-COG-$FA_{1.0}$ alone. We interpreted this as essentially complete displacement of FA by $G5_{Ac}$-COG-$FA_{1.0}$ in the FBP binding pocket by the 10-fold stronger binder. The addition of another 14 equivalents of FA, to give a 28-fold excess of FA over dendrimer conjugate, failed to displace $G5_{Ac}$-COG-$FA_{1.0}$ from FBP. Thus, the COG linked conjugation of FA to G5 PAMAM successfully created a stronger binder to the FBP protein that acts via dendrimer binding to the FBP surface outside of the FA binding pocket, i.e. an exosite binding interaction. As illustrated in Figure 1.1, the nearest region showing extensive FBP surface structural change is the β–sheet region and this appears to be likeliest dendrimer/protein binding site. However, the 30 kDa dendrimer is similar in size to FBP and binding to the induced α-helix or other protein surface sites cannot be ruled out. For this system, a synergistic interaction between the dendrimer and the protein affords tight binding.

We also explored competitive binding of FA/FBP and $G5_{Ac}$-$FITC_{1.9}$-$FA_{4.4}$/FBP. In this instance, the tryptophan fluorescence and FITC fluorescence can be observed in separate channels. Both tryptophan and FITC fluorescence are quenched upon mixing 100 nM $G5_{Ac}$-$FITC_{1.9}$-$FA_{4.4}$ with 58nM FBP (Figure 1.6, red curves). Upon addition of 100 nM FA, a small amount of additional quenching is observed consistent with the initial sub-stoichiometric treatment of FBP with $G5_{Ac}$ -$FITC_{1.9}$-$FA_{4.4}$ (Figure 1.6a, blue curve). This evidence, coupled with strong quenching observed by $G5_{Ac}$-COG-$FA_{1.0}$, provides additional support for the conclusion that the multiple FAs present on $G5_{Ac}$ -$FITC_{1.9}$-$FA_{4.4}$ do not generate additional FBP quenching, and therefore binding, and that the multiple FA ligands are not generating interactions with multiple proteins. On the other hand, the FITC fluorescence increases upon addition of excess FA. This suggests that $G5_{Ac}$-$FITC_{1.9}$-$FA_{4.4}$ is bound more weakly than $G5_{Ac}$-COG-$FA_{1.0}$ as it is displaced by excess FA. The Stern-Volmers analysis of $G5_{Ac}$ -$FITC_{1.9}$-$FA_{4.4}$ showed this material quenches a similar fraction of accessible fluorophores (f_a= 57 ± 2%) as compared to FA (f_a = 67 ± 3%) with a slightly smaller dissociation constant of K_D = 16.0 ± 1.9nM as opposed to K_D = 27.9 ± 3.3nM from FA.

The $G5_{Ac}$-COG-$FA_{1.0}$/FBP binding kinetics were studied under *pseudo*-first order conditions by mixing 1-20 nM $G5_{Ac}$-COG-$FA_{1.0}$ into a 58 nM FBP solution. The fluorescence changes were followed over 1-2 hours until equilibrium was reached (Figure 1.7 inset). The resulting curves were fit to single exponentials to obtain k_{obs} for each concentration. k_{obs} was fit as a function of $G5_{Ac}$-COG-$FA_{1.0}$ concentration to the equation below that describes a two-step tight binding SOTB model. In the equation, we use P* to

indicate a change in protein structure, a common feature of the SOTB model, and L* to indicate the change in dendrimer structure as highlighted in Figure 1.1.

$$P + L \underset{k_{-1}}{\overset{k_1}{\rightleftharpoons}} P\text{-}L \underset{k_{-2}}{\overset{k_2}{\rightleftharpoons}} P^*\text{-}L^*$$

$$k_{obs} = \frac{k_2[L]}{K_D + [L]} + k_{-2}$$

The fit provided a K_D value of 9.9 ± 8.5 nM, a k_2 value of 0.07 ± 0.02 s^{-1}, and a k_{-2} value of 0.008 ± 0.007 s^{-1} (Figure 1.7). Recall the K_D value obtained from the modified Stern-Volmer analysis was 2.4 ± 0.2nM. These two values agree well with each other. The rate constant k_2 indicates a slow onset binding interaction between the dendrimer and protein.

Conclusions

Substrate-triggered polymer binding to an FBP exosite gives an order of magnitude greater binding constant than that obtained by the native FA ligand. In addition, FA-triggered exosite binding is not displaced by presence of a 28-fold excess of free FA. Tight polymer-protein binding, triggered by specific

Figure 1.7. Binding kinetics between $G5_{Ac}$-COG-$FA_{1.0}$ and FBP. k_{obs} values were obtained by fitting the curves obtained for the addition of 1, 2, 5, 10, and 20 nm solution of $G5_{Ac}$-COG-$FA_{1.0}$ to 58 nM FBP (pH 7.4, 1x PBS solution). Inset: Change in fluorescence over time for addition of 2nM $G5_{Ac}$-COG-$FA_{1.0}$.

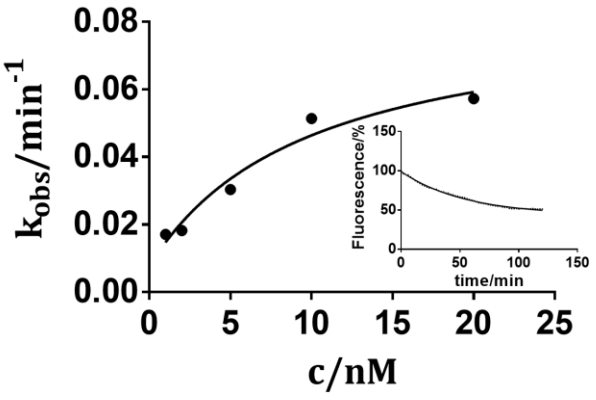

ligand binding, provides promising strategy for binding scaffolds containing drugs and/or imaging agents to desired protein targets.

Bibliography

1. Larson, N.; Ghandehari, H., Polymeric Conjugates for Drug Delivery. *Chem. Mater.* **2012,** *24* (5), 840-853.
2. Duncan, R.; Gaspar, R., Nanomedicine(s) under the Microscope. *Molecular Pharmaceutics* **2011,** *8* (6), 2101-2141.
3. Srinivasarao, M.; Galliford, C. V.; Low, P. S., Principles in the design of ligand-targeted cancer therapeutics and imaging agents. *Nat. Rev. Drug. Discov.* **2015,** *14* (3), 203-219.
4. Li, W.; Zhan, P.; De Clercq, E.; Lou, H.; Liu, X., Current drug research on PEGylation with small molecular agents. *Prog. Plym. Sci.* **2013,** *38* (3-4), 421-444.
5. van Dongen, M.; Dougherty, C. A.; Banaszak Holl, M. M., Multivalent Polymers for Drug Delivery and Imaging: The Challenges of Conjugation. *Biomacromolecules* **2014,** *15*, 3215-3234.
6. Roglin, L.; Lempens, E. H. M.; Meijer, E. W., A Synthetic "Tour de Force": Well-Defined Multivalent and Multimodal Dendritic Structures for Biomedical Applications. *Angew. Chem., Int. Ed.* **2011,** *50* (1), 102-112.
7. Low, P. S.; Henne, W. A.; Doorneweerd, D. D., Discovery and development of folic-acid-based receptor targeting for Imaging and therapy of cancer and inflammatory diseases. *Acc. Chem. Res.* **2008,** *41* (1), 120-129.
8. York, A. W.; Zhang, Y.; Holley, A. C.; Guo, Y.; Huang, F.; McCormick, C. L., Facile Synthesis of Multivalent Folate-Block Copolymer Conjugates via Aqueous RAFT Polymerization: Targeted Delivery of siRNA and Subsequent Gene Suppression. *Biomacromolecules* **2009,** *10* (4), 936-943.
9. Zong, H.; Thomas, T. P.; Lee, K. H.; Desai, A. M.; Li, M. H.; Kotlyar, A.; Zhang, Y.; Leroueil, P. R.; Gam, J. J.; Banaszak Holl, M. M.; Baker, J. R., Jr., Bifunctional PAMAM dendrimer conjugates of folic acid and methotrexate with defined ratio. *Biomacromolecules* **2012,** *13* (4), 982-91.
10. Chen, C.; Ke, J.; Zhou, X. E.; Yi, W.; Brunzelle, J. S.; Li, J.; Young, E.-L.; Xu, H. E.; Melcher, K., Structural basis for molecular recognition of folic acid by folate receptors. *Nature* **2013,** *500*, 486-490.
11. Kamen, B. A., Folate Receptors and Therapeutic Applications. In *Targeted Drug Strategies for Cancer and Inflammation*, Jackman, A. L.; Leamon, C. P., Eds. Springer: 2011.
12. Hoier-Madsen, M.; Holm, J.; Hansen, S. I., Alpha isoforms of soluble and membrane-linked folate-binding protein in human blood. *Bioscience Rep.* **2008,** *28* (3), 153-160.
13. Ghitis, J., Folate Binding in Milk. *Am. J. Clin. Nutr.* **1967,** *20*, 1-4.
14. Antony, A. C., Folate receptors. *Annu. Rev. Nutr.* **1996,** *16*, 501-521.
15. Henderson, G. B., Folate Binding Proteins. *Annu. Rev. Nutr.* **1990,** *10* (319-335).

16. Holm, J.; Babol, L. N.; Markova, N.; Lawaetz, A. J.; Hansen, S. I., The interrelationship between ligand binding and thermal unfolding of the folate binding protein. The role of self-association and pH. *BBA-Proteins Proteom* **2014,** *1844* (3), 512-519.
17. Holm, J.; Bruun, S. W.; Hansen, S. I., The Complex Interplay Between Ligand Binding and Conformational Structure of the Folate Binding Protein (Folate Receptor): Biological Perspectives. *BBA-Proteins Proteom* **2015**, *1854*, 1249-1259.
18. Wibowo, A. S.; Singh, M.; Reeder, K. M.; Carter, J. J.; Kovach, A. R.; Meng, W. Y.; Ratnam, M.; Zhang, F. M.; Dann, C. E., Structures of human folate receptors reveal biological trafficking states and diversity in folate and antifolate recognition. *Proc. Natl. Acad. Sci. USA* **2013,** *110* (38), 15180-15188.
19. van Dongen, M. A.; Desai, A.; Orr, B. G.; Baker, J. R.; Banaszak Holl, M. M., Quantitative Analysis of Generation and Branch Defects in G5 Poly(amidoamine) Dendrimer. *Polymer* **2013,** *54*, 4126-4133.
20. van Dongen, M. A.; Silpe, J. E.; Dougherty, C. A.; Kanduluru, A. K.; Choi, S. K.; Orr, B. G.; Low, P. S.; Banaszak Holl, M. M., Avidity Mechanism of Dendrimer-Folic Acid Conjugates. *Molec. Pharm.* **2014,** *11*, 1696-1706.
21. Mullen, D. G.; McNerny, D. Q.; Desai, A.; Cheng, X. M.; DiMaggio, S. C.; Kotlyar, A.; Zhong, Y.; Qin, S.; Kelly, C. V.; Thomas, T. P.; Majoros, I.; Orr, B. G.; Baker, J. R.; Holl, M. M. B., Design, Synthesis, and Biological Functionality of a Dendrimer-Based Modular Drug Delivery Platform. *Bioconjugate Chem.* **2011,** *22* (4), 679-689.
22. Majoros, I. J.; Thomas, T. P.; Mehta, C. B.; Baker, J. R., Poly(amidoamine) Dendrimer-Based Multifunctional Engineered Nanodevice for Cancer Therapy. *J. Med. Chem.* **2005,** *48*, 5892-5899.
23. Treloar, T.; Grieve, P. A.; Nixon, P. F., One-step Affinity Purification of Folate-Binding Protein, a minor whey protein. *Aust. J. Dairy Tech.* **2000,** *59*, 96.
24. Hong, S.; Leroueil, P. R.; Majoros, I.; Orr, B. G.; Baker, J. R.; Banaszak Holl, M. M., The Binding Avidity of a Nanoparticle-Based Multivalent Targeted Drug Delivery Platform. *Chemistry and Biology* **2007,** *14*, 107-115.
25. Leroueil, P. R.; DiMaggio, S.; Leistra, A. N.; Blanchette, C. D.; Orme, C.; Sinniah, K.; Orr, B. G.; Banaszak Holl, M. M., Characterization of Folic Acid and Poly(amidoamine) Dendrimer Interactions with Folate Binding Protein: A Force-Pulling Study. *J. Phys. Chem. B* **2015,** *119* (35), 11506-11512.
26. Wei, Q.; Becherer, T.; Angioletti-Uberti, S.; Dzubiella, J.; Wischke, C.; Neffe, A. T.; Lendlein, A.; Ballauff, M.; Haag, R., Protein Interactions with Polymer Coatings and Biomaterials. *Angew. Chem. Int. Ed.* **2014,** *53* (31), 8004-8031.
27. Hattori, T.; Hallberg, R.; Dubin, P. L., Roles of Electrostatic Interaction and Polymer Structure in the Binding of β-Lactoglobulin to Anionic Polyelectrolytes: Measurement of Binding Constants by Frontal Analysis Continuous Capillary Electrophoresis. *Langmuir* **2000,** *16* (25), 9738-9743.
28. Browne, M. M.; Lubarsky, G. V.; Davidson, M. R.; Bradley, R. H., Protein adsorption onto polystyrene surfaces studied by XPS and AFM. *Surf. Sci.* **2004,** *553* (1–3), 155-167.
29. Hicks, T. M.; Verbeek, C. J. R.; Lay, M. C.; Manley-Harris, M., Changes in hydrogen bonding in protein plasticized with triethylene glycol. *J. Appl. Polym. Sci.* **2015,** *132* (26).

30. Miura, Y., Design and synthesis of well-defined glycopolymers for the control of biological functionalities. *Polym. J.* **2012,** *44* (7), 679-689.
31. Silpe, J. E.; Sumit, M.; Thomas, T. P.; Huang, B.; Kotlyar, A.; van Dongen, M.; Banaszak Holl, M. M.; Orr, B. G.; Choi, S. K., Avidity Modulation of Folated-Targeted Multivalent Dendrimers for Evaluating Biophysical Models of Cancer Targeting Nanoparticles. *ACS Chem. Biol.* **2013,** *8*, 2063-2071.
32. Kukowska-Latallo, J. F.; Candido, K. A.; Cao, Z. Y.; Nigavekar, S. S.; Majoros, I. J.; Thomas, T. P.; Balogh, L. P.; Khan, M. K.; Baker, J. R., Nanoparticle targeting of anticancer drug improves therapeutic response in animal model of human epithelial cancer. *Cancer Res.* **2005,** *65* (12), 5317-5324.
33. Chen, Y.; Cao, W.; Zhou, J.; Pidhatika, B.; Xiong, B.; Huang, L.; Tian, Q.; Shu, Y.; Wen, W.; Hsing, I. M.; Wu, H., Poly(L-lysine)-graft-folic acid-coupled poly(2-methyl-2-oxazoline) (PLL-g-PMOXA-c-FA): A Bioactive Copolymer for Specific Targeting to Folate Receptor-Positive Cancer Cells. *Acs Appl. Mater. Interfaces* **2015,** *7* (4), 2919-2930.
34. Sunoqrot, S.; Bugno, J.; Lantvit, D.; Burdette, J. E.; Hong, S., Prolonged blood circulation and enhanced tumor accumulation of folate-targeted dendrimer-polymer hybrid nanoparticles. *J. Controlled Rel.* **2014,** *191*, 115-122.
35. Knight, C. G., Fluorimetric assays of proteolytic enzymes. *Methods Enzymol.* **1995,** *248*, 18-34.
36. Lakowicz, J. R., *Principles of Fluorescence Spectroscopy*. 3rd ed.; Springer: New York, 2006.
37. Samworth, C. M.; Esposti, M. D.; Lenaz, G., Quenching of the intrinsic tryptophan fluorescence of mitochondrial ubiquinol—cytochrome-c reductase by the binding of ubiquinone. *Eur. J. Biochem.* **1988,** *171* (1-2), 81-86.
38. Eftink, M. R., Fluorescence methods for studying equilibrium macromolecule-ligand interactions. *Methods Enzymol.* **1997,** *278*, 221-57.
39. Kranz, D. M.; Patrick, T. A.; Brigle, K. E.; Spinella, M. J.; Roy, E. J., Conjugates of folate and anti-T-cell-receptor antibodies specifically target folate-receptor-positive tumor cells for lysis. *Proc. Natl. Acad. Sci.* **1995,** *92* (20), 9057-9061.

Chapter II

Nanoparticle Agglomeration Triggered by Protein Aggregation

Introduction

Folate receptor-targeted nanoparticles have been widely employed as a tumor targeting strategy for imaging and drug delivery applications.[1-10] Conjugation of folic acid (FA) to small molecule drugs and nanoparticles provides a convenient, cheap, and chemically stable cancer targeting vector. Despite substantial promise and seven clinical trials to date,[11] neither molecular nor nanoparticulate FA conjugates have reached the clinic, suggesting challenges to their use *in vivo*. Herein, we focus on interactions of FA with serum folate binding protein (FBP) and how these interactions may impact the use of FA as a targeted delivery agent.

It is well established that FA induces the aggregation of several proteins in serum, notably albumin, lactoferrin, and FBP.[12-18] We have previously noted that FA-dendrimer conjugates can lead to strong binding interactions between the polymer and FBP surface[19] and that FA, methotrexate (MTX), and leucovorin all increase the aggregation propensity of FBP.[18] Furthermore, FA- and MTX-polymer conjugates induce substantially more fluorescence quenching of FBP than FA or MTX alone, indicating that the conjugates are affecting protein structure and potentially aggregation behavior.[20] For these reasons, we decided to explore the role of FA-induced FBP aggregation in causing the agglomeration of FA-conjugated nanoparticles. The formation of agglomerated particles and the masking

of the conjugated FA by FBP binding is likely to play an important role in transport and other *in vivo* behavior of FA-conjugated materials.

For this initial study we selected the well-studied class of iron oxide particles (IOP) that have been explored for imaging and drug delivery applications.[21-24] IOPs have been extensively investigated for imaging and drug delivery due to their low toxicity, biocompatibility, large surface area, and suitable magnetic properties. IOP-based agents in the 30 – 300 nm diameter size range have been approved for clinical use, and additional materials are currently in clinical trials.[25] Particles under consideration have sizes ranging from 20 nm to 3500 nm in diameter.[26] The majority of them are administered via intravenous injection. However, it is known that IOPs, especially unmodified ones, are prone to agglomeration and even precipitation in physiological environment.[27] Therefore, investigation of IOP agglomeration in the presence of serum proteins is crucial when evaluating the safety and efficacy of these nanoparticles.

Folic acid conjugated iron oxide nanoparticles were synthesized to study particle agglomeration in the presence of FBP and albumin (Figure 2.1). It was found that self-aggregation of FBP upon FA binding further triggers the agglomeration of the IOP particles. Considering the drastically smaller size of protein compared to the iron oxide particles, this aggregation-agglomeration event resembles a biological cascade – a small initial event (ligand-protein binding) leading to larger effects (protein structural rearrangement), that then leads to protein aggregation and particle agglomeration. The agglomerates formed are orders of magnitude larger in size than the initiating small molecule. Two iron oxide-FA conjugates, a ~40 nm FA-IOP and a ~450 nm FA-SeraMag, were selected for use in this study to model the range of particle sizes applied in the clinic. In particular, the ~40 nm

IOP represents a class of SPIONs (superparamagnetic iron oxide nanoparticles) that is a commonly used nanoparticle platform for drug conjugation and the development of targeted theranostics.[28-30] The ~450 nm SeraMag is a commercially available particle widely used in protein separation and preparation.[31-33] The two IOPs allow us to contrast the behavior of particles designed for very different applications, which highlights both different surface chemistry and size range.

The FA-conjugated beads were mixed with human serum albumin (HSA) and folate binding protein (FBP) at the physiological concentration of these serum proteins. At 2 nM FBP with 0.01% w/w 40 nm particles in 1x PBS buffer (28 nM nominally), the cascade resulted in agglomeration to form 3800 ± 1100 nm diameter particles. Similarly, at 2 nM FBP with 0.01% w/w 450 nm particles (SeraMag) in 1x PBS buffer (16 pM nominally), agglomeration resulted in 4030 ± 1100 nm diameter particles. Albumin, the most abundant serum protein, had no significant impact on ~40 nm FA-IOP particle agglomeration up to the micromolar level; however, it did inhibit the agglomeration of the ~450 nm FA-SeraMag particles. In addition to dynamic light scattering (DLS), atomic force microscopy (AFM) was carried out to study the morphology of agglomerated particles.

Experimental Section

Materials The ~450 nm amine-blocked iron oxide beads were obtained from GE healthcare (Sera-Mag SpeedBeads Amine-Blocked Particles, 10 mg/mL). The ~40 nm iron oxide particles functionalized by polyethylene glycol(PEG-2k) with amine terminal groups were obtained from Ocean NanoTech. All other chemicals were purchased from Sigma Aldrich if not otherwise specified. The folate binding protein was isolated and purified as previously reported.[2]

Folic acid conjugation to magnetic beads

Folic acid was conjugated to the beads via an EDC-NHS carbodiimide coupling procedure. Specifically, 300 μL MilliQ water, 34 μL folic acid solution (3.9 mg dissolved in 1 mL DMSO, then diluted 100x by MilliQ water), 51.7 μL NHS solution (17.9 mg N-Hydroxysuccinimide in 100 mL MilliQ water), 35.9 μL EDC solution (4.0 mg 1-Ethyl-3-(3-dimethylaminopropyl) carbodiimide in 100 mL MiliQ water) and 578.4 μL MilliQ water were added into a vial for carboxylate activation. The vial was transferred to a shaker (23 °C, 115 rpm) for 7h (credit: Sarah Klem, Alexis K Jones).

1% Magnetic bead stock solutions containing 0.05% sodium azide were vortexed and 1 mL was pipetted into a vial and placed on a magnet for about 3 min. The stock buffer was discarded and the beads washed with MilliQ water twice. The beads were re-suspended into the activation solution described above and allowed to react for 12 hrs. The beads were then washed with water and characterized by IR spectroscopy.

AFM experiment

Protein solutions are made in filtered 1x PBS at their corresponding physiological concentration: 2 nM for FBP. The 1% conjugated beads stock solution was added into the protein solution to make a final concentration of 0.01% w/w. 40 μL of the resulting solution was spin coated at 4,200 rpm onto a freshly cleaved mica surface. The sample was further rinsed with another 40 μL milliQ water while spinning to rinse any remaining salt from the surface. PBS salts crystals can occasionally be found on the mica surface but they have dramatically different morphology from the IOP particles. AFM imaging was carried out in tapping mode using PicoPlus 5500 (Agilent Electronic Measurement, Aspire CT300R

tip) and NanoIR-2 (Anasys, Anasys PR-EX-T125-10 tip) AFM systems. For the ~ 40 nm FA-IOP the particle size is similar to the nominal 10 nm tip radius. Tip deconvolution was done to better estimate the particle diameter ($d=d_c^2/8R$, where d is the particle diameter, d_c is the observed diameter, and R is the tip radius).

DLS experiment

The sample solutions were prepared as describe for the AFM experiments. DLS was performed on a Nanosizer ZS (Malvern Instruments Ltd.) instrument. The DLS in figure 2.2 and figure 2.4 was taken right after FBP addition into the solution. Additional DLS experiments on agglomerate particle stability were also taken under same conditions (Figures S7). The solutions were measured in a 1 mL cuvette at 25 °C. The refractive index and absorption coefficient for the particles were set at 2.42 and 0.01, respectively. All data is an average of 15 scans.

Results and Discussion

Folic acid modification on IOP surfaces has widely been used as a targeting strategy in drug development. The surface modification of folic acid on IOP may influence the interactions of the particles with serum proteins in a nonspecific fashion due to its

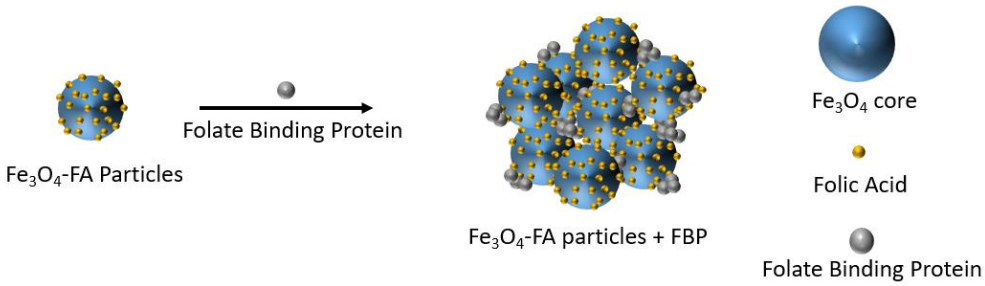

Figure 2.1. A target-ligand triggered biological cascade. Addition of a physiological concentration of folate binding protein (2 nM FBP) triggers the agglomeration of the large folic acid conjugated iron oxide particles in 1x PBS, even with the presence of a high concentration of human serum albumin.

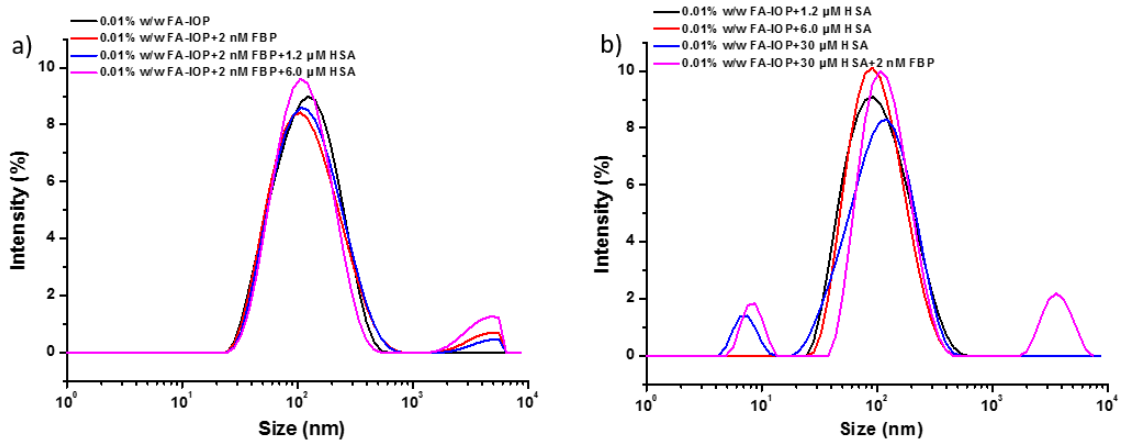

Figure 2.2. Agglomeration of ~40 nm FA-IOP triggered by FBP binding and aggregation as measured by DLS: a) 0.01% w/w FA-IOP + 2 nM FBP followed by addition of HSA. b) 0.01% w/w FA-IOP + HSA followed by addition of 2 nM FBP.

hydrophobicity and in a specific fashion due to FA-FBP interactions. Both of these interactions have the potential to lead to particle agglomeration in the blood serum.

FBP and albumin are the proteins primarily responsible for the binding and transportation of folates in blood serum.[34] FBP exists at a 1-2 nM concentration in human serum whereas the much more abundant human serum albumin (HSA) is present at 30 µM.[35] FBP binds to FA tightly with a nanomolar dissociation constant, and the protein self-aggregates upon substrate binding.[2, 14] Crystallographic studies indicate that FBP forms a beta sheet upon folic acid binding and it is hypothesized that this contributes to the aggregation of the protein. [20] This observation led us to wonder if the protein-protein aggregation could also trigger the agglomeration of large FA conjugated particles. FBP aggregation is stable at pH 6-9 and at temperatures ranging from 20°C to 37°C.[16, 36] HSA is a ~40,000 times weaker binder for folate as compared to FBP.[37] However, it composes more than half of total serum proteins and is also involved in folate transportation and regulation in blood.

In this study, two iron oxide particles are coated with FA via EDC/NHS coupling as a model system for folic acid-targeted nanomedicine. The particles were characterized using infrared spectroscopy. The ~40 nm FA-IOP IR spectrum has peaks at 2916 cm^{-1} and 2851 cm^{-1}, which correspond to the CH_2 stretching vibrations for the polyethyleneglycol (PEG) surface coating on iron oxide nanoparticles.[38] An FA carbonyl stretch, 1646 cm^{-1} for free FA, is observed at 1632 cm^{-1} for conjugated FA-IOP. A strong peak at 983 cm^{-1} is also indicative of FA and shifts to 1004 cm^{-1} upon conjugation. The FA-SeraMag showed a peak at 1560 cm^{-1} in the IR spectrum, which is also detected in the unconjugated SeraMag IR spectrum. An FA carbonyl stretch appears at 1654 cm^{-1} in the conjugated particle and appears to provide an increase in intensity in that region. A strong peak at 989 cm-1 is also observed for conjugated material.

DLS and AFM were employed to study the agglomeration of particles induced by serum protein binding. A 0.01% w/w FA- conjugated nanoparticle (FA-IOP and FA-SeraMag) solution was mixed with serum proteins at their physiological concentration. All the solutions were made in 1x PBS buffer to mimic the salt environment in blood serum. The 0.01% w/w (28 nM nominally) ~40 nm FA-IOP aqueous 1X PBS solution yielded one peak with a number weighted average diameter at 39 ± 13 nm (Figure 2.2a). Upon mixing with 2 nM FBP, a peak centered at 3800 ± 1100 nm was detected. The resulting agglomerate is nearly 100-fold larger in diameter (10^6 larger in volume) than the original particle. Addition of up to 6 μM HSA into this solution did not have a significant impact on the DLS signal. This process was also studied in reverse: HSA was added to the FA-IOP solution prior to FBP addition. At 30 μM HSA, the particles have a measured diameter of 42 ± 13 nm (Figure 2.2b). The hydrodynamic size of HSA monomer is also detected

under this condition at 7.0 ± 1.4 nm, which is in agreement with the literature value.[39, 40] These data indicate the HSA non-specific binding on this particle is minimal. Addition of 2 nM FBP into this FA-IOP/HSA solution generated agglomerated particles with a diameter of 3100 ± 850 nm, and zeta potential of 4.7 ± 0.3mV. These data indicate that HSA does not trigger a cascade and that excess HSA does not inhibit particle agglomeration upon the addition of FBP.

In order to obtain information about particle morphology, the solutions were spin coated onto a cleaved mica surface and characterized using tapping mode AFM (Figure 2.3). The 0.01% w/w FA-IOP particles alone demonstrated a well-dispersed non-agglomerated pattern on the mica surface with an average diameter of 59 ± 7 nm (Figure

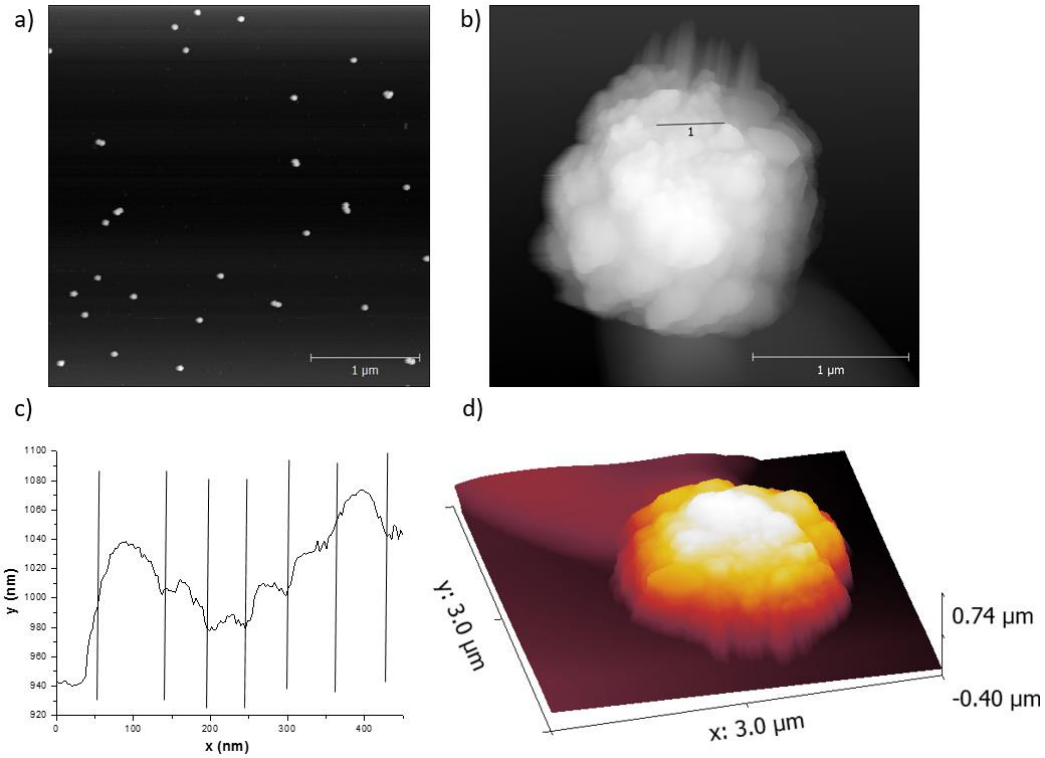

Figure 2.3. AFM image of the ~40 nm FA-IOP mixed with FBP. a) 0.01% w/w FA-IOP without FBP b) A typical agglomerated particle at 0.01% w/w FA-IOP + 2 nM FBP c) Line scan profile of the agglomerated particles. The particle surface can be sectioned into ~50 nm spheres d) 3D rendering of an agglomerated particle.

2.3a). This diameter was corrected to 44 ± 10 nm after tip deconvolution. FBP-assisted particle agglomeration was observed by AFM once the 0.01% w/w FA-IOP particle was mixed with 2 nM FBP. An average of five agglomerates yielded a particle volume of 58 ± 1.9 μm^3 (equivalent to ~210,000 ~40 nm FA-IOP particles), corresponding to an average diameter of ~ 2400 ± 800 nm. The particle diameter falls into the size range measured by DLS (Figure 2.3b). The large particle agglomerates featured a rough surface consisting of distinct particles and line scan profiles demonstrated the existence of ~50 nm particles on the agglomerate surface (Figure 2.3c). The size of the smaller components in the line scan is consistent with the size of individual FA-IOP particles. A 3D rendering of the aggregated particle is illustrated in Figure 2.3d. The small FA-IOP particles on the surface can be easily seen in the large agglomerated particle. For the HSA containing samples, the high HSA concentration resulted in a multi-layer protein coating on the mica surface and this prevented measurement of the IOP aggregates.

The much larger FA-SeraMag particle (450 ± 70nm) was also titrated with FBP and HSA under similar conditions (Figure 2.4a). The addition of 2 nM FBP to form a 0.01% w/w solution (16 pM nominally) shifted the entire peak to 4030 ± 1100 nm with a measured zeta potential of 1.5 ± 0.2 mV. The original peak for the 450 nm particles was no longer observable. This indicates a full agglomeration of particles in the presence of 2 nM FBP. This full shift of the peak is most likely due to the much higher protein to particle molarity ratio in this case. For each ~450 nm FA-SeraMag particle there were 125 FBP protein added whereas for each ~40 nm FA-IOP there were just 0.07 FBP (*i.e.*, 14 IOP per FBP). On the other hand, 600 µM (40 g/L) HSA lead to a two-fold increase in diameter (880 ± 360 nm). This could be due to nonspecific binding from HSA and formation of a protein

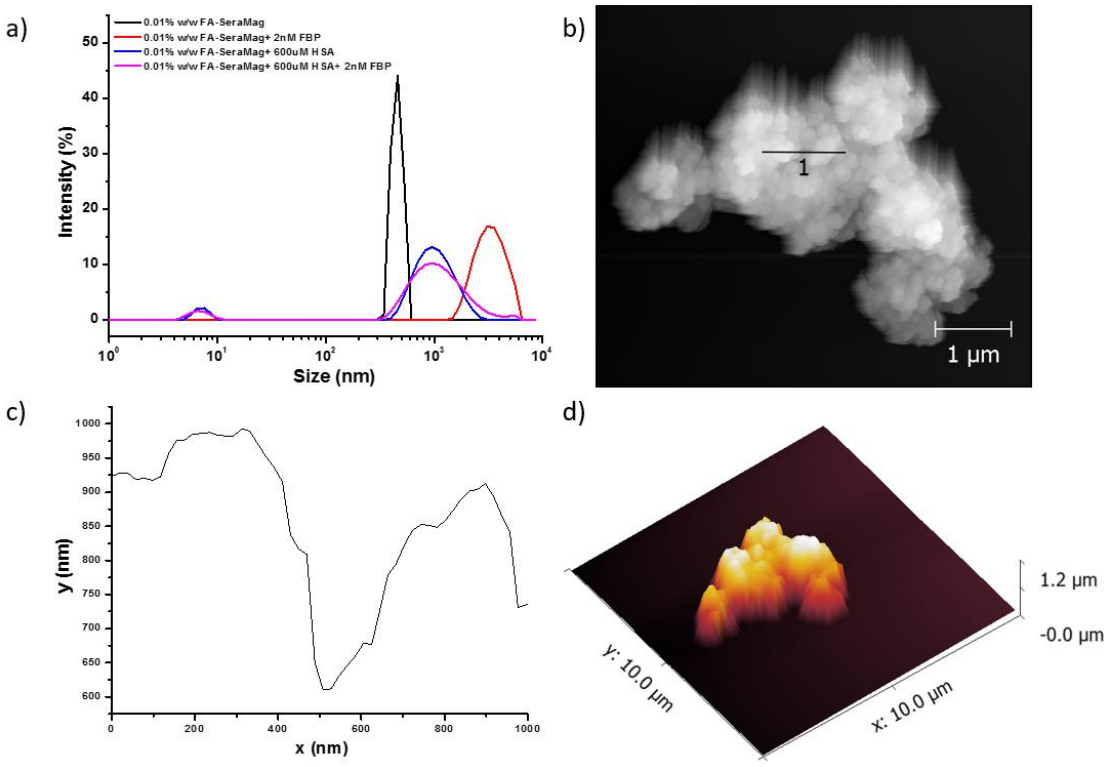

Figure 2.4. a) Agglomeration of the ~450 nm FA-IOP triggered by FBP binding and aggregation as measured by DLS. b) AFM image of 0.01% w/w FA-SeraMag mixed with 2nM FBP. c) Line scan profile of the agglomerated particles. The particle surface is composed of ~500nm spheres d) 3D image of the agglomerated particles.

corona at this concentration. Addition of 2 nM FBP into this solution did not introduce a full shift of this ~880 nm particle to a large agglomeration as was the case without HSA. However, the peak associated with the ~880 nm particle exhibits tailing (Figure 2.4a, pink) up to a diameter of ~3200 nm. It is worth noting that in the presence of HSA only a small fraction of FA-SeraMag particles shifted to the large agglomeration and this differs substantially from the addition of FBP alone. This leads us to hypothesize that the HSA protein corona could be protecting the FA-SeraMag particles from agglomeration. The FBP assisted particle agglomeration was measured by AFM for solutions containing 0.01% w/w FA-SeraMag particle mixed with 2 nM FBP (Figures 4b, S5). The large agglomerate featured a rough surface and the line scan profile demonstrated the existence of ~500 nm particles (Figure 2.4c). This result indicates that the large particle agglomerate is composed of the smaller FA-SeraMag components. A 3D rendering of the agglomerated particle is also shown in Figure 2.4d. In this case, the average agglomerate contains ~360 FA-SeraMag particles. A summary of DLS size measurement for both IOPs is provided in Table I.

Table I. Number weighted average particle diameter from DLS			
Sample	# weighted average Ave. Dia. Peak 1 /nm	# weighted average Ave. Dia. Peak 2 /nm	# weighted average Dia. Peak 3 /nm
0.01% w/w FA-IOP	-	39 ± 13	-
0.01% w/w FA-IOP + 2nM FBP	-	39 ± 13	3800 ± 1100
0.01% w/w FA-IOP + 30 µM HSA	7.3 ± 1.5	42 ± 13	-
0.01% w/w FA-IOP + 30 µM HSA+ 2nM FBP	7.0 ± 1.4	54 ± 10	3100 ± 850
0.01% w/w FA-SeraMag	-	450 ± 70	-
0.01% w/w FA-SeraMag + 2nM FBP	-	-	4030 ± 1100
0.01% w/w FA-SeraMag + 600µM HSA	6.4 ± 1.0	880 ± 360	-
0.01% w/w FA-SeraMag + 600µM HSA+ 2nM FBP	6.3 ± 0.9	840 ± 330	-

The FBP-induced agglomeration of the ~40 nm and ~450 nm IOP resembles a biological cascade in two ways. First, there are three discrete steps (ligand binding, protein structural change, protein self-aggregation) preceding the fourth step (particle agglomeration). Second, the initial interaction occurs on a small scale (small molecule interaction with the protein binding pocket). This small interaction triggers a series of changes that results in agglomeration of the much larger ~40 nm and ~450 nm IOP.

Under the physiological concentrations employed, HSA is in large excess to the IOPs. However, HSA does not bind to FA as tightly as FBP. The combination of these two factors results in a substantial amount of free HSA left in solution. The non-specific binding

of HSA to the surface conjugated FA does not introduce a structural change in HSA that can induce IOP agglomeration. However, addition of 2 nM FBP into the ~40 nm IOP-HSA solution does generate particle agglomeration. This shows that physiological concentrations of FBP trigger can particle agglomeration even in the presence of the large concentration of HSA found physiologically. HSA on the particle may make the surface less accessible to FBP and provide some protection to IOP particle from agglomeration and this is observed for the ~450 nm IOP where there is a much higher HSA concentration per particle.[41]

Particle size can have a significant impact on tissue distribution *in vivo*. Particles larger than 2000 nm accumulate readily in the spleen and liver. Particles ranging from 100 nm and 200 nm have been shown to escape liver and spleen filtration, while small nanoparticles are filtered out by the kidneys.[42] For the iron oxide particles in this study, physiological concentrations of FBP triggered the agglomeration of FA-IOP in the presence of HSA and altered them from ~ 40 nm diameter particles that could readily transport through tissue into ~3000-4000 nm diameter particles that would be incapable of tissue penetration and would be trafficked to spleen and liver. The result illustrates the importance of considering serum protein-induced particle agglomeration when designing FA-targeted systems.

Conclusion

Nano-engineered drug delivery platforms have received great attention in the past decade as therapeutic and diagnostic tools.[3, 43-49] In order to best understand the safety and efficacy of these targeted nanomaterials *in vivo*, previous studies have explored the interactions with serum proteins.[41, 50-52] It is widely proposed that the absorbed protein layer

on nanomaterials influences the bio-identity and therein the transportation and uptake of the nanomaterial into target cells.[53-56] Future *in vitro* studies of the nanomaterial interaction with serum proteins, and the resulting effect on cellular uptake, will play an essential role in understanding the pathology of these materials. In the work described here, folic acid-conjugated iron oxide nanoparticles, initiate a set of interactions with serum proteins that leads to particle agglomeration. Additional work is needed to fully understand the implications of this agglomeration for biological trafficking and potential health risks.[57-63]

Bibliography

1. Vlahov, I. R.; Leamon, C. P., (2012) Engineering Folate–Drug Conjugates to Target Cancer: From Chemistry to Clinic. *Bioconjug. Chem.* 23, 1357-1369.
2. Chen, J.; van Dongen, M. A.; Merzel, R. L.; Dougherty, C. A.; Orr, B. G.; Kanduluru, A. K.; Low, P. S.; Marsh, E. N.; Banaszak Holl, M. M., (2016) Substrate-Triggered Exosite Binding: Synergistic Dendrimer/Folic Acid Action for Achieving Specific, Tight-Binding to Folate Binding Protein. *Biomacromolecules* 17, 922-927.
3. Sonvico, F.; Mornet, S.; Vasseur, S.; Dubernet, C.; Jaillard, D.; Degrouard, J.; Hoebeke, J.; Duguet, E.; Colombo, P.; Couvreur, P., (2005) Folate-Conjugated Iron Oxide Nanoparticles for Solid Tumor Targeting as Potential Specific Magnetic Hyperthermia Mediators: Synthesis, Physicochemical Characterization, and in Vitro Experiments. *Bioconjug. Chem.* 16, 1181-1188.
4. Jiang, Q. L.; Zheng, S. W.; Hong, R. Y.; Deng, S. M.; Guo, L.; Hu, R. L.; Gao, B.; Huang, M.; Cheng, L. F.; Liu, G. H.; Wang, Y. Q., (2014) Folic acid-conjugated Fe3O4 magnetic nanoparticles for hyperthermia and MRI in vitro and in vivo. *Appl. Surf. Sci.* 307, 224-233.
5. Dong, S.; Cho, H. J.; Lee, Y. W.; Roman, M., (2014) Synthesis and Cellular Uptake of Folic Acid-Conjugated Cellulose Nanocrystals for Cancer Targeting. *Biomacromolecules* 15, 1560-1567.
6. Yin, F.; Zhang, B.; Zeng, S.; Lin, G.; Tian, J.; Yang, C.; Wang, K.; Xu, G.; Yong, K.-T., (2015) Folic acid-conjugated organically modified silica nanoparticles for enhanced targeted delivery in cancer cells and tumor in vivo. *J. Mater. Chem. B* 3, 6081-6093.
7. Li, J.; Zheng, L.; Cai, H.; Sun, W.; Shen, M.; Zhang, G.; Shi, X., (2013) Polyethyleneimine-mediated synthesis of folic acid-targeted iron oxide nanoparticles for in vivo tumor MR imaging. *Biomaterials* 34, 8382-8392.
8. Zhang, Z.; Hu, Y.; Yang, J.; Xu, Y.; Zhang, C.; Wang, Z.; Shi, X.; Zhang, G., (2016) Facile Synthesis of Folic Acid-Modified Iron Oxide Nanoparticles for Targeted MR Imaging in Pulmonary Tumor Xenografts. *Molecular Imaging and Biology* 18, 569-578.
9. Shi, X.; Wang, S. H.; Swanson, S. D.; Ge, S.; Cao, Z.; Van Antwerp, M. E.; Landmark, K. J.; Baker, J. R., (2008) Dendrimer-Functionalized Shell-crosslinked Iron

Oxide Nanoparticles for In-Vivo Magnetic Resonance Imaging of Tumors. *Adv. Mater. (Weinheim, Ger.)* 20, 1671-1678.
10. Wang, S. H.; Shi, X.; Van Antwerp, M.; Cao, Z.; Swanson, S. D.; Bi, X.; Baker, J. R., (2007) Dendrimer-Functionalized Iron Oxide Nanoparticles for Specific Targeting and Imaging of Cancer Cells. *Adv. Funct. Mater.* 17, 3043-3050.
11. Lutz, R. J., (2015) Targeting the folate receptor for the treatment of ovarian cancer. *Transl. Cancer. Res.* 4, 118-126.
12. Jha, N. S.; Kishore, N., (2011) Thermodynamic studies on the interaction of folic acid with bovine serum albumin. *J. Chem. Thermodyn.* 43, 814-821.
13. Tavares, G. M.; Croguennec, T.; Lê, S.; Lerideau, O.; Hamon, P.; Carvalho, A. F.; Bouhallab, S., (2015) Binding of Folic Acid Induces Specific Self-Aggregation of Lactoferrin: Thermodynamic Characterization. *Langmuir* 31, 12481-12488.
14. Merzel, R. L.; Chen, J.; Marsh, E. N. G.; Banaszak Holl, M. M., (2015) Folate binding protein-Outlook for drug delivery applications. *Chin. Chem. Lett.* 26, 426-430.
15. Holm, J.; Lawaetz, A. J.; Hansen, S. I., (2012) Ligand binding induces a sharp decrease in hydrophobicity of folate binding protein assessed by 1-anilinonaphthalene-8-sulphonate which suppresses self-association of the hydrophobic apo-protein. *Biochem. Biophys. Res. Commun.* 425, 19-24.
16. Pedersen, T.; Svendsen, I.; Hansen, S.; Holm, J.; Lyngbye, J., (1980) Aggregation of a folate-binding protein from cow's milk. *Carlsberg Res. Commun.* 45, 161-166.
17. Bruun, S. W.; Holm, J.; Hansen, S. I.; Andersen, C. M.; Norgaard, L., (2009) A chemometric analysis of ligand-induced changes in intrinsic fluorescence of folate binding protein indicates a link between altered conformational structure and physico-chemical characteristics. *Appl. Spectrosc.* 63, 1315-1322.
18. Merzel, R. L.; Boutom, S. M.; Chen, J.; Frey, C.; Shedden, K.; Marsh, E. N. G.; Banaszak Holl, M. M., Folate binding protein: Therapeutic natural nanotechnology for folic acid, methotrexate, and leucovorin. *In Press*.
19. van Dongen, M. A.; Silpe, J. E.; Dougherty, C. A.; Kanduluru, A. K.; Choi, S. K.; Orr, B. G.; Low, P. S.; Banaszak Holl, M. M., (2014) Avidity Mechanism of Dendrimer–Folic Acid Conjugates. *Mol. Pharm.* 11, 1696-1706.
20. Chen, C.; Ke, J.; Zhou, X. E.; Yi, W.; Brunzelle, J. S.; Li, J.; Yong, E.-L.; Xu, H. E.; Melcher, K., (2013) Structural basis for molecular recognition of folic acid by folate receptors. *Nature* 500, 486-489.
21. Zhao, M.; Li, A.; Chang, J.; Fu, X.; Zhang, Z.; Yan, R.; Wang, H.; Liang, S., (2013) Develop a novel superparamagnetic nano-carrier for drug delivery to brain glioma. *Drug Deliv* 20, 95-101.
22. Pala, K.; Serwotka, A.; Jelen, F.; Jakimowicz, P.; Otlewski, J., (2014) Tumor-specific hyperthermia with aptamer-tagged superparamagnetic nanoparticles. *Int. J. Nanomedicine* 9, 67-76.
23. Li, J.; He, Y.; Sun, W.; Luo, Y.; Cai, H.; Pan, Y.; Shen, M.; Xia, J.; Shi, X., (2014) Hyaluronic acid-modified hydrothermally synthesized iron oxide nanoparticles for targeted tumor MR imaging. *Biomaterials* 35, 3666-3677.
24. Bogdanov, A. A.; Dixon, A. J.; Gupta, S.; Zhang, L.; Zheng, S.; Shazeeb, M. S.; Zhang, S.; Klibanov, A. L., (2016) Synthesis and Testing of Modular Dual-Modality Nanoparticles for Magnetic Resonance and Multispectral Photoacoustic Imaging. *Bioconjug. Chem.* 27, 383-390.

25. Jin, R.; Lin, B.; Li, D.; Ai, H., (2014) Superparamagnetic iron oxide nanoparticles for MR imaging and therapy: design considerations and clinical applications. *Curr. Opin. Pharmacol.* 18, 18-27.
26. Leung, K., Ferumoxides. In *Molecular Imaging and Contrast Agent Database (MICAD)*, National Center for Biotechnology Information (US): Bethesda (MD), 2004.
27. Paul, K. G.; Frigo, T. B.; Groman, J. Y.; Groman, E. V., (2004) Synthesis of ultrasmall superparamagnetic iron oxides using reduced polysaccharides. *Bioconjug. Chem.* 15, 394-401.
28. Duan, H.; Kuang, M.; Wang, X.; Wang, Y. A.; Mao, H.; Nie, S., (2008) Reexamining the Effects of Particle Size and Surface Chemistry on the Magnetic Properties of Iron Oxide Nanocrystals: New Insights into Spin Disorder and Proton Relaxivity. *The Journal of Physical Chemistry C* 112, 8127-8131.
29. Mahmoudi, M.; Sant, S.; Wang, B.; Laurent, S.; Sen, T., (2011) Superparamagnetic iron oxide nanoparticles (SPIONs): Development, surface modification and applications in chemotherapy. *Adv. Drug Delivery Rev.* 63, 24-46.
30. Xu, H.; Aguilar, Z. P.; Yang, L.; Kuang, M.; Duan, H.; Xiong, Y.; Wei, H.; Wang, A., (2011) Antibody conjugated magnetic iron oxide nanoparticles for cancer cell separation in fresh whole blood. *Biomaterials* 32, 9758-9765.
31. Dorgan, L.; Magnotti, R.; Hou, J.; Engle, T.; Ruley, K.; Shull, B., (1999) Methods to determine biotin-binding capacity of streptavidin-coated magnetic particles. *J. Magn. Magn. Mater.* 194, 69-75.
32. Lenglet, L., (2009) Multiparametric magnetic immunoassays utilizing non-linear signatures of magnetic labels. *J. Magn. Magn. Mater.* 321, 1639-1643.
33. Sato, A. K.; Sexton, D. J.; Morganelli, L. A.; Cohen, E. H.; Wu, Q. L.; Conley, G. P.; Streltsova, Z.; Lee, S. W.; Devlin, M.; DeOliveira, D. B.; Enright, J.; Kent, R. B.; Wescott, C. R.; Ransohoff, T. C.; Ley, A. C.; Ladner, R. C., (2002) Development of Mammalian Serum Albumin Affinity Purification Media by Peptide Phage Display. *Biotechnol. Prog.* 18, 182-192.
34. Turek, J. J.; Leamon, C. P.; Low, P. S., (1993) Endocytosis of folate-protein conjugates: ultrastructural localization in KB cells. *J. Cell Sci.* 106, 423-430.
35. Henderson, G. B., (1990) Folate-binding proteins. *Annu. Rev. Nutr.* 10, 319-335.
36. Hansen, S. I.; Holm, J.; Lyngbye, J.; Pedersen, T. G.; Svendsen, I., (1983) Dependence of aggregation and ligand affinity on the concentration of the folate-binding protein from cow's milk. *Arch. Biochem. Biophys.* 226, 636-642.
37. Soliman, H. A.; Olesen, H., (1976) Folic acid binding by human plasma albumin. *Scand. J. Clin. Lab. Invest.* 36, 299-304.
38. Sharifi, S.; Daghighi, S.; Motazacker, M. M.; Badlou, B.; Sanjabi, B.; Akbarkhanzadeh, A.; Rowshani, A. T.; Laurent, S.; Peppelenbosch, M. P.; Rezaee, F., (2013) Superparamagnetic iron oxide nanoparticles alter expression of obesity and T2D-associated risk genes in human adipocytes. *Sci. Rep.* 3, 2173.
39. Zhou, C.; Qi, W.; Neil Lewis, E.; Carpenter, J. F., (2015) Concomitant Raman spectroscopy and dynamic light scattering for characterization of therapeutic proteins at high concentrations. *Anal. Biochem.* 472, 7-20.
40. Hushcha, T. O.; Luik, A. I.; Naboka, Y. N., (2000) Conformation changes of albumin in its interaction with physiologically active compounds as studied by quasi-elastic light scattering spectroscopy and ultrasonic method. *Talanta* 53, 29-34.

41. Wells, M. A.; Abid, A.; Kennedy, I. M.; Barakat, A. I., (2012) Serum proteins prevent aggregation of Fe(2)O(3) and ZnO nanoparticles. *Nanotoxicology* 6, 837-846.
42. Longmire, M.; Choyke, P. L.; Kobayashi, H., (2008) Clearance properties of nano-sized particles and molecules as imaging agents: considerations and caveats. *Nanomedicine (Lond)* 3, 703-717.
43. Zhang, H.; Li, J.; Hu, Y.; Shen, M.; Shi, X.; Zhang, G., (2016) Folic acid-targeted iron oxide nanoparticles as contrast agents for magnetic resonance imaging of human ovarian cancer. *J. Ovarian Res.* 9, 19.
44. Li, J.; Hu, Y.; Yang, J.; Sun, W.; Cai, H.; Wei, P.; Sun, Y.; Zhang, G.; Shi, X.; Shen, M., (2015) Facile synthesis of folic acid-functionalized iron oxide nanoparticles with ultrahigh relaxivity for targeted tumor MR imaging. *J. Mater. Chem. B* 3, 5720-5730.
45. Shevtsov, M. A.; Nikolaev, B. P.; Yakovleva, L. Y.; Marchenko, Y. Y.; Dobrodumov, A. V.; Mikhrina, A. L.; Martynova, M. G.; Bystrova, O. A.; Yakovenko, I. V.; Ischenko, A. M., (2014) Superparamagnetic iron oxide nanoparticles conjugated with epidermal growth factor (SPION-EGF) for targeting brain tumors. *Int. J. Nanomedicine* 9, 273-287.
46. Kanwar, J. R.; Kamalapuram, S. K.; Krishnakumar, S.; Kanwar, R. K., (2016) Multimodal iron oxide (Fe3O4)-saturated lactoferrin nanocapsules as nanotheranostics for real-time imaging and breast cancer therapy of claudin-low, triple-negative (ER-/PR-/HER2-). *Nanomedicine* 11, 249-268.
47. Zheng, H.; Xiao, M.; Yan, Q.; Ma, Y.; Xiao, S.-J., (2014) Small Circular DNA Molecules Act as Rigid Motifs To Build DNA Nanotubes. *J. Am. Chem. Soc.* 136, 10194-10197.
48. Landmark, K. J.; DiMaggio, S.; Ward, J.; Kelly, C.; Vogt, S.; Hong, S.; Kotlyar, A.; Myc, A.; Thomas, T. P.; Penner-Hahn, J. E.; Baker, J. R.; Holl, M. M. B.; Orr, B. G., (2008) Synthesis, Characterization, and in Vitro Testing of Superparamagnetic Iron Oxide Nanoparticles Targeted Using Folic Acid-Conjugated Dendrimers. *ACS Nano* 2, 773-783.
49. Zwicke, G. L.; Mansoori, G. A.; Jeffery, C. J., (2012) Utilizing the folate receptor for active targeting of cancer nanotherapeutics. *Nano Reviews* 3, 10.3402/nano.v3403i3400.18496.
50. Walkey, C. D.; Olsen, J. B.; Guo, H.; Emili, A.; Chan, W. C., (2012) Nanoparticle size and surface chemistry determine serum protein adsorption and macrophage uptake. *J. Am. Chem. Soc.* 134, 2139-2147.
51. Lartigue, L.; Wilhelm, C.; Servais, J.; Factor, C.; Dencausse, A.; Bacri, J.-C.; Luciani, N.; Gazeau, F., (2012) Nanomagnetic Sensing of Blood Plasma Protein Interactions with Iron Oxide Nanoparticles: Impact on Macrophage Uptake. *ACS Nano* 6, 2665-2678.
52. Dominguez-Medina, S.; Kisley, L.; Tauzin, L. J.; Hoggard, A.; Shuang, B.; D. S. Indrasekara, A. S.; Chen, S.; Wang, L.-Y.; Derry, P. J.; Liopo, A.; Zubarev, E. R.; Landes, C. F.; Link, S., (2016) Adsorption and Unfolding of a Single Protein Triggers Nanoparticle Aggregation. *ACS Nano* 10, 2103-2112.
53. Paula, A. J.; Araujo Júnior, R. T.; Martinez, D. S. T.; Paredes-Gamero, E. J.; Nader, H. B.; Durán, N.; Justo, G. Z.; Alves, O. L., (2013) Influence of Protein Corona on the Transport of Molecules into Cells by Mesoporous Silica Nanoparticles. *ACS Appl. Mater. Interfaces* 5, 8387-8393.

54. Tenzer, S.; Docter, D.; Kuharev, J.; Musyanovych, A.; Fetz, V.; Hecht, R.; Schlenk, F.; Fischer, D.; Kiouptsi, K.; Reinhardt, C.; Landfester, K.; Schild, H.; Maskos, M.; Knauer, S. K.; Stauber, R. H., (2013) Rapid formation of plasma protein corona critically affects nanoparticle pathophysiology. *Nat. Nano* 8, 772-781.
55. Landgraf, L.; Christner, C.; Storck, W.; Schick, I.; Krumbein, I.; Dähring, H.; Haedicke, K.; Heinz-Herrmann, K.; Teichgräber, U.; Reichenbach, J. R.; Tremel, W.; Tenzer, S.; Hilger, I., (2015) A plasma protein corona enhances the biocompatibility of Au@Fe3O4 Janus particles. *Biomaterials* 68, 77-88.
56. Sakulkhu, U.; Mahmoudi, M.; Maurizi, L.; Salaklang, J.; Hofmann, H., (2014) Protein Corona Composition of Superparamagnetic Iron Oxide Nanoparticles with Various Physico-Chemical Properties and Coatings. *Sci. Rep.* 4, 5020.
57. Oberdörster, G., (2010) Safety assessment for nanotechnology and nanomedicine: concepts of nanotoxicology. *J. Intern. Med.* 267, 89-105.
58. Hock, S. C.; Ying, Y. M.; Wah, C. L., (2011) A review of the current scientific and regulatory status of nanomedicines and the challenges ahead. *PDA J. Pharm. Sci. Technol.* 65, 177-195.
59. Gosens, I.; Post, J. A.; de la Fonteyne, L. J. J.; Jansen, E. H. J. M.; Geus, J. W.; Cassee, F. R.; de Jong, W. H., (2010) Impact of agglomeration state of nano- and submicron sized gold particles on pulmonary inflammation. *Part. Fibre. Toxicol.* 7, 1-11.
60. Alcantara, D.; Lopez, S.; García-Martin, M. L.; Pozo, D., (2016) Iron oxide nanoparticles as magnetic relaxation switching (MRSw) sensors: Current applications in nanomedicine. *Nanomedicine: Nanotech. Bio.l Med.* 12, 1253-1262.
61. Wu, Z.; Li, W.; Webley, P. A.; Zhao, D., (2012) General and Controllable Synthesis of Novel Mesoporous Magnetic Iron Oxide@Carbon Encapsulates for Efficient Arsenic Removal. *Adv. Mater. (Weinheim, Ger.)* 24, 485-491.
62. Liu, G.; Gao, J.; Ai, H.; Chen, X., (2013) Applications and Potential Toxicity of Magnetic Iron Oxide Nanoparticles. *Small* 9, 1533-1545.
63. Yildirimer, L.; Thanh, N. T. K.; Loizidou, M.; Seifalian, A. M., (2011) Toxicology and clinical potential of nanoparticles. *Nano Today* 6, 585-607.

Chapter III.

Multi-scale Anterior Cruciate Ligament Microdamage due to Normal Mechanical Loading

Introduction

The anterior cruciate ligament (ACL) is a key connective tissue stabilizing the knee. Over 200,000 ACL injuries occur annually in the US[1]. The lifetime public health burden of ACL tears in the US was estimated to be $7.6 billion annually when treated with reconstruction and $17.7 billion annually when treated with rehabilitation.[1] The number of ACL reconstructions in the US is growing rapidly with an estimated annual increase between 3.4% and 7.7%.[2-4] Among them, nearly three quarters of ACL injuries follow a non-contact mechanism even in the high contact sport of NFL football.[5] However, the cause of non-contact ACL injuries remains somewhat of an enigma. Several theories have been proposed to explain the mechanism of non-contact ACL injury, including aggressive quadriceps loading,[6] excessive joint compressive loading,[7] awkward landing or decelerating gestures,[8] and neuromuscular control deficit.[9]

Current orthopedic studies focus mainly on the acute triggers of the injury, per the traditional view of the non-contact ACL injury. Very few studies have been conducted to explore the development of pre-injury ACL damage under repetitive loading. In this study, we ask one key question: What level of damage, if any, would the human ACL sustain under *routine* mechanical loading? If the knee joint experiences 2-3 times body weight

during normal walking[10] and 3-4.5 times body weight during light sport activities such as jogging, golf and tennis.[11, 12] In previous studies, Wojtys et al have demonstrated *in vitro* that the ACL could experience fatigue failure in fewer than 100 repeated landings with limited internal femoral rotation.[13] The characterization of ACL damage from those loading tests is the major focus of this paper.

In this study, the ACL microdamage produced in cadaveric knees was visualized and evaluated at multiple levels from molecular, fibril, and tissue levels. Molecular level ACL damage was investigated using both IR spectroscopy and fluorescent collagen hybridizing peptide (CHP) probes. In the IR spectroscopy, an amide I peak shift from 1664 cm^{-1} to 1740 cm^{-1} is closely associated with ligament collagen damage. The TAMRA dye conjugated fluorescent CHP probe can detect the molecular level unwinding of collagen after mechanical testing.[14] Fibril level collagen damage was investigated using atomic force microscopy (AFM). Fibril voids at nanometer scale ranging from 10 nm to 100 nm were observed after mechanical testing. Tissue level collagen damage was studied using second harmonic generation. The mechanically tested tissue demonstrated larger fibril voids compared to the untested control. Only one knee tested in this study led to complete mechanical failure after loading but they all demonstrated different levels of microdamage across all scales.

The combination of these techniques allowed systematic investigation of the ACL microdamage under repeated loading. This microdamage helps deepen the understanding of process of pre-fracture ACL fatigue. Eventually this understanding would help guide the development, preventive training and treatment plans for athletes and active people.

Experimental Section

ACL sample preparation

The cadaveric knees are tested on a custom-built apparatus to simulate repeated single-leg pivot landings as described in previous report.[15] One knee from each pair was set aside as an internal control. After mechanical testing, the ACL explant was extracted and cut in half longitudinally. Each half was embedded in a water-soluble mounting medium SCEM (Super Cryo Embedding Medium, Section Lab). The embedded tissues (both tested and control) were sectioned using a tungsten carbide blade (Leica, #TC-65) under -25 ℃ (Leica cryostat model 3050S, 8°, 20 μm). The sectioned tissue was transferred to adhesive tapes using the Kowamoto method.[16, 17] The sectioned sample slices were stored in a moisturized chamber under -20℃ until being imaged.

AFM-IR data collection

The sectioned sample slices were immersed in deionized water to remove the embedding media and keep the sample hydrolyzed. The tape containing the ACL enthesis was cut to a ~2cm square and glued to a stainless-steel AFM sample puck. The AFM-IR data was collected using a NanoIR2 system (Anasys Instruments). For a typical IR map, the images are taken at 2*2 μm^2, co-average 256x, power 2.07% and trace speed 0.1Hz.

SHG and fluorescence data collection

The samples are stained with a CHP-TAMRA dye after the AFM-IR imaging. The peptide sequence can be found from the previous publication.[14] The peptide was synthesized by Pierce Custom Peptides. The TAMRA fluorophore was picked so the fluorescence is not overlapping with the sample autofluorescence or the SHG signal. Before peptide staining, 25 μL CHP stock solution (150 μM) was heated under 80 ℃ for

10min to deaggregate the peptide. The solution was quenched by immersion in 4 ℃ water for 15 seconds. The aliquot was diluted to a total volume of 500 μL and dropped onto the ACL slice. The sample was incubated in dark in a 4 ℃ fridge overnight. The sample was rinsed with 1mL PBS three times before immersed in oil (Leica type F) for microscopic imaging. The images are collected using a Leica SP8 confocal microscopy system. The light source was a 910nm IR laser (10% LP, 33% gain, 38% offset, pinhole wide open). Two PMT detectors are set at 440nm for the detection of SHG forward/backward signal. The fluorescence signal was detected at a 570-590 nm window.

Results and Discussion

Fibril damage detected by AFM-IR

Atomic force microscopy is a common tool of studying the collagen order and morphology at nano meter scale. The AFM images from the failed patient ACL and the mechanically tested cadaveric ACL were compared (figure 3.1). This data showed fibril voids ranging from 20 nm to 150 nm on both types of tissues. The fibril voids appear as the dark spheres on the AFM images. The fibril voids sizes are very similar between the case of the failed patient ACL and the mechanically tested cadaver ACL. These sphere patterns were not observed on the untested cadaveric control. The size range of those fibril voids falls into the size range for collagen fibrils. It is possible that individual collagen fibril on the ligament was pulled out during the mechanical testing and subsequently leaving the fibril voids on the ligament.

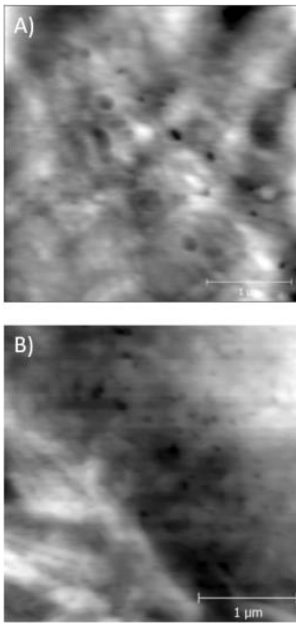

Figure. 3.1. AFM height images of voids in ligament associated with mechanically induced microdamage. A) Failed patient ACL, B) Mechanically tested cadaver ACL.

Figure. 3.2. AFM-IR spectra from the ligament of A) explant from mechanically tested cadaveric ACL, B) explant from patient having failed ACL, C) explanted of untested cadaveric ACL.

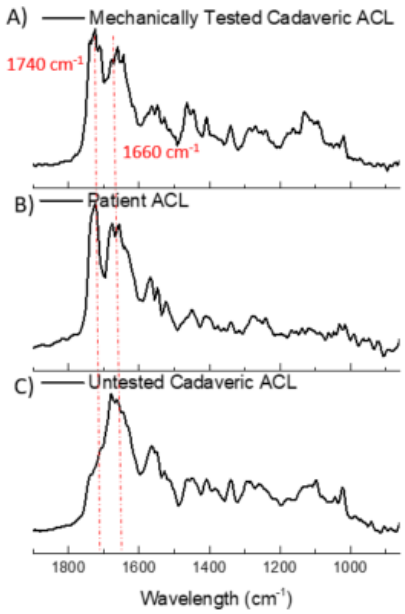

Additionally, on the AFM-IR system, an enhanced 1740 cm^{-1} peak was detected on the spectrum of the mechanically tested sample (figure 3.2). This peak is shifted from the collagen amide I peak at 1660 cm^{-1} and this 1740 cm^{-1} peak can also be reversibly created by dehydrating/rehydrating the collagen tissue. This disordered collagen peak can also be observed on the fractured patient ACL and is not present on the untested cadaveric ACL control. This IR peak demonstrated the microdamage on the ACL could be deeper into the molecular level and at a scale even smaller than the fibril level damage as detected by the AFM technique. This peak is indicating the unwinding of the collagen fibril is happening when the ACL was mechanically tested under submaximal loading.

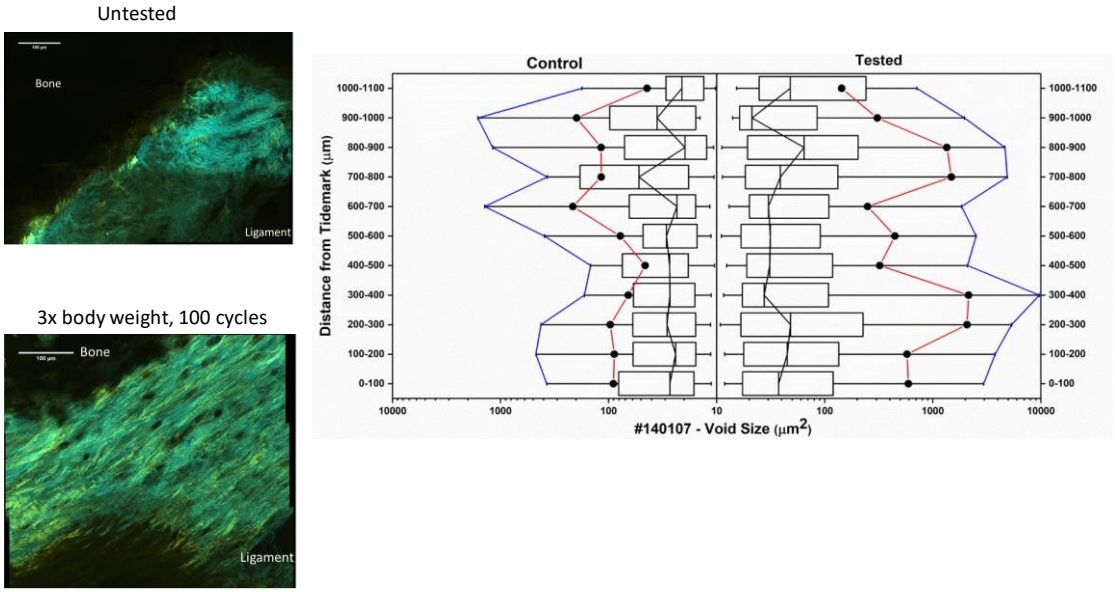

Figure 3.3. fibril void on ligament detected by SHG.

Fibril damage detected by SHG and confocal microscopy

Collagen molecules are well aligned biopolymers and can be specifically detected by second harmonic generation. SHG imaging showed fibril voids at the micrometer scale (figure 3.3). The tested ACL demonstrated the spherical fibril voids. Fibril void analysis on the sectioned ACL showed that the collagen SHG fibril voids on the tested ACL is approximately ten times larger than the control ACL (figure 3.3 right). Additionally, the samples are incubated with TAMRA conjugated collagen hybrid peptide (CHP) to detect the molecular level damage. The CHP has a complementary sequence to the collagen and can bind specifically to the unwound collagen molecules. The conjugated TAMRA dye on the peptide has a red fluorescence that is away from the autofluorescence and the TAMRA intensity could be the indication of molecular level collagen damage. The tested ACL sample demonstrated an increased TAMRA fluorescence hence higher CHP binding

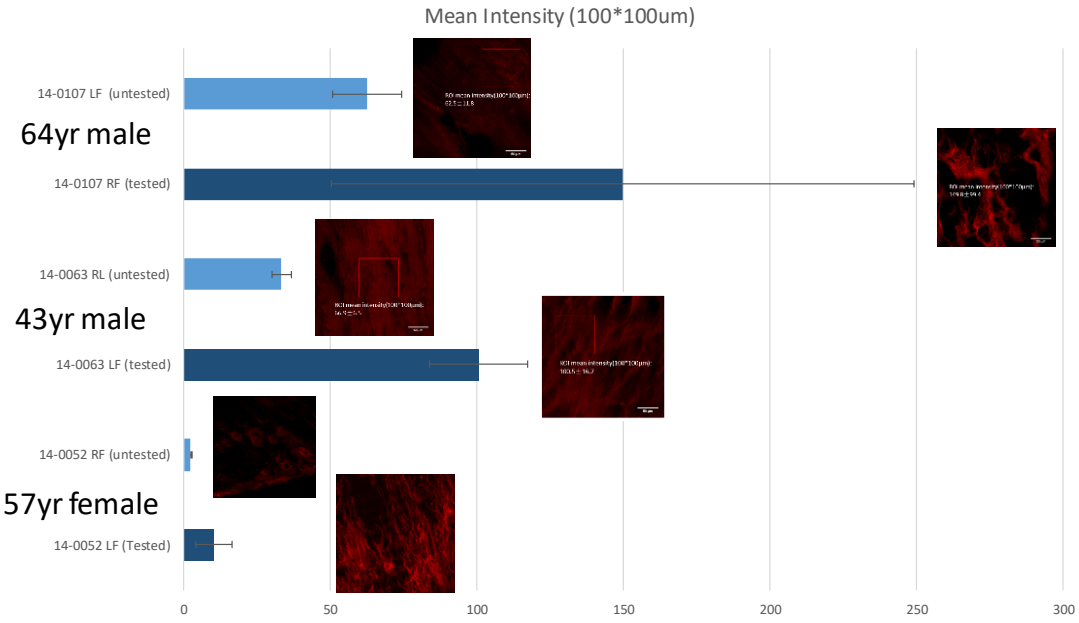

Figure 3.4. collagen disordering detected by CHP-TAMRA.

towards the ACL (figure 3.4). This is consistent with the IR data demonstrating the molecular level damage of the ACL after the mechanical testing.

Conclusion

This study demonstrated the evidence of the hierarchical ACL damages at different scales after the mechanical testing. The fibril and fiber voids observed on AFM and SHG resembles the voids observed on fractured ACL. These results support the hypothesis that the microdamages can result from normal mechanical loading and eventually become a risk factor for ACL injuries. More cadaveric data and the comparison between the cadaver and patient could help develop further understanding of the non-contact ACL damages.

Bibliography

1. Mather, R. C., 3rd; Koenig, L.; Kocher, M. S.; Dall, T. M.; Gallo, P.; Scott, D. J.; Bach, B. R., Jr.; Spindler, K. P., (2013) Societal and economic impact of anterior cruciate ligament tears. *J Bone Joint Surg Am* 95, 1751-1759.
2. Leathers, M. P.; Merz, A.; Wong, J.; Scott, T.; Wang, J. C.; Hame, S. L., (2015) Trends and Demographics in Anterior Cruciate Ligament Reconstruction in the United States. *J Knee Surg* 28, 390-394.
3. Kim, S.; Bosque, J.; Meehan, J. P.; Jamali, A.; Marder, R., (2011) Increase in outpatient knee arthroscopy in the United States: a comparison of National Surveys of Ambulatory Surgery, 1996 and 2006. *J Bone Joint Surg Am* 93, 994-1000.
4. Collins, J. E.; Katz, J. N.; Donnell-Fink, L. A.; Martin, S. D.; Losina, E., (2013) Cumulative incidence of ACL reconstruction after ACL injury in adults: role of age, sex, and race. *Am. J. Sports Med.* 41, 544-549.
5. Boden, B. P.; Dean, G. S.; Feagin, J. A., Jr.; Garrett, W. E., Jr., (2000) Mechanisms of anterior cruciate ligament injury. *Orthopedics* 23, 573-578.
6. Houde, D.; Berkowitz, S. A.; Engen, J. R., (2011) The utility of hydrogen/deuterium exchange mass spectrometry in biopharmaceutical comparability studies. *J. Pharm. Sci.* 100, 2071-2086.
7. Meyer, E. G.; Baumer, T. G.; Slade, J. M.; Smith, W. E.; Haut, R. C., (2008) Tibiofemoral contact pressures and osteochondral microtrauma during anterior cruciate ligament rupture due to excessive compressive loading and internal torque of the human knee. *Am. J. Sports Med.* 36, 1966-1977.

8. Boden, B. P.; Torg, J. S.; Knowles, S. B.; Hewett, T. E., (2009) Video analysis of anterior cruciate ligament injury: abnormalities in hip and ankle kinematics. *Am. J. Sports Med.* 37, 252-259.
9. Hewett, T. E.; Di Stasi, S. L.; Myer, G. D., (2013) Current concepts for injury prevention in athletes after anterior cruciate ligament reconstruction. *Am. J. Sports Med.* 41, 216-224.
10. D'Lima, D. D.; Fregly, B. J.; Patil, S.; Steklov, N.; Colwell, C. W., (2012) Knee joint forces: prediction, measurement, and significance. *Proceedings of the Institution of Mechanical Engineers. Part H, Journal of Engineering in Medicine* 226, 95-102.
11. Cleather, D. J.; Goodwin, J. E.; Bull, A. M. J., (2013) Hip and knee joint loading during vertical jumping and push jerking. *Clin. Biomech.* 28, 98-103.
12. D'Lima, D. D.; Steklov, N.; Patil, S.; Colwell, C. W., (2008) The Mark Coventry Award: In Vivo Knee Forces During Recreation and Exercise After Knee Arthroplasty. *Clinical Orthopaedics and Related Research* 466, 2605-2611.
13. Lipps, D. B.; Wojtys, E. M.; Ashton-Miller, J. A., (2013) Anterior cruciate ligament fatigue failures in knees subjected to repeated simulated pivot landings. *Am J Sports Med* 41, 1058-1066.
14. Zitnay, J. L.; Li, Y.; Qin, Z.; San, B. H.; Depalle, B.; Reese, S. P.; Buehler, M. J.; Yu, S. M.; Weiss, J. A., (2017) Molecular level detection and localization of mechanical damage in collagen enabled by collagen hybridizing peptides. *Nature Communications* 8, 14913.
15. Beaulieu, M. L.; Wojtys, E. M.; Ashton-Miller, J. A., (2015) Risk of Anterior Cruciate Ligament Fatigue Failure Is Increased by Limited Internal Femoral Rotation During In Vitro Repeated Pivot Landings. *The American journal of sports medicine* 43, 2233-2241.
16. Kawamoto, T.; Kawamoto, K., (2014) Preparation of thin frozen sections from nonfixed and undecalcified hard tissues using Kawamot's film method (2012). *Methods Mol. Biol.* 1130, 149-164.
17. Kawamoto, T., (2003) Use of a new adhesive film for the preparation of multi-purpose fresh-frozen sections from hard tissues, whole-animals, insects and plants. *Arch. Histol. Cytol.* 66, 123-143.

Conclusions and Future Directions

The substrate-triggered polymer binding to an FBP exosite provides a new protein binding strategy. The polymer scaffold can not only act as the drug delivery vector, but also the booster for protein binding affinities. This design strategy may not be limited to the design to FBP binders. This strategy could save a lot resources in the new drug design and be resistant to single site protein mutation. The protein surface and polymer surface interaction may be the most important factor to consider in such design. The FBP triggered nanoparticle agglomeration could pose a risk factor in the targeted drug development. How these nanoparticles interact with other serum proteins, and the lipid in the blood serum, would be the next question to answer. These works could help further understand the implications of this agglomeration for biological trafficking and potential health risks.

For the ACL project, the evidence has been accumulating that the microdamage to the ACL occurs after the mechanical loading at the ACL without the presence of ACL fracture. The next step is to understand how the ACL fractures develop overtime when people age and ACL become repetitively loaded. A diagnostic tool, such as a SHG or fluorescence endoscope, can be developed to help the clinicians to better illustrate the development of the ACL injury. These tools could also help the improvement of exercising and training practices to better protect the ACL of athletes or common people.